

POLITECNICO DI TORINO



Collegio di Ingegneria Meccanica, Aerospaziale, del Veicolo e della  
Produzione

Corso di Laurea Magistrale in Ingegneria Aerospaziale

Tesi di Laurea Magistrale

# Emission Imaging of a Coaxial Single Element GOX/GH<sub>2</sub> Rocket Combustion Chamber

**Relatore**

Prof. Dario Giuseppe Pastrone

**Co-Relatore**

M. Sc. Fernanda Winter

**Autore**

Graziano Laera

Marzo 2018



## Declaration of Authorship

Name: **Graziano Laera**

I hereby declare that this thesis is my own work prepared without the help of a third party. No other than the listed literature and resources have been used. All sources transferred literally or analogously to this work have been labeled accordingly.

Additionally, I hereby certify that this thesis has not been underlain in any other examination procedure up to the present.

Date:

Signature:



*A Filmia e alla mia famiglia*



# Acknowledgments

I would like to thank Fernanda Winter for welcoming me warmly in this new world and for making me discover how it is, seen closely and touched by hand, the world of scientific research. Thank you for your daily patience and for the availability offered in every circumstance. The evenings spent in the laboratory were used to understand that sacrifices are necessary to achieve results. My thanks to Professor Dario G. Pastrone for giving me the chance to live this new life experience. Thanks also to Professor Oskar J. Haidn and the Lehrstuhl für Flugantriebe of the Technische Universität München for giving me the opportunity to prove myself in a such stimulating field.

I would like to thank Filmia, for always being present and for making me grow as a man. Even if physically distant, your spirit has always been beside me. You are my everyday strength and the engine that drives me to move forward. You know.

Also a thank you to my old friends with whom I lived and still live the most fun and magical moments of my life.

Finally, my family. Annamaria, Piero and Giovanna. Because without a family so caring and close and without your sacrifices, all this could not have happened. We made it, together. Thank you from the bottom of my heart. And i would also like to extend my thanks to my grandparents, indispensable support for my growth, and to my uncles, especially Uncle Francesco, always available to give me a ride in the car to Bari at the time of departures, and likewise to come and pick me up at the time of returns.



# Ringraziamenti

Vorrei ringraziare Fernanda Winter per avermi accolto calorosamente in questo nuovo mondo e per avermi fatto scoprire com'è fatto, visto da vicino e toccato con mano, il mondo della ricerca scientifica. Grazie per la tua pazienza quotidiana e per la disponibilità offerta in ogni circostanza. Le serate trascorse in laboratorio sono servite a capire che i sacrifici sono necessari per ottenere risultati. Ringrazio il professor Dario G. Pastrone per avermi dato la possibilità di vivere questa nuova esperienza. Grazie anche al professor Oskar J. Haidn e al Lehrstuhl für Flugantriebe of the Technische Universität München per avermi dato l'opportunità di mettermi alla prova in un campo così stimolante.

Vorrei ringraziare Filmia, per essere sempre stata presente e per avermi fatto crescere come uomo. Anche se fisicamente distante, il tuo spirito mi è stato sempre accanto. Sei la mia forza quotidiana e il motore che mi spinge ad andare avanti.

Un ringraziamento anche ai miei vecchi amici con cui ho vissuto e vivo tuttora i momenti più magici e divertenti della mia vita.

Infine, la mia famiglia. Annamaria, Piero e Giovanna. Perché senza una famiglia così premurosa e vicina e senza i vostri sacrifici, tutto questo non sarebbe potuto accadere. Ce l'abbiamo fatta, insieme. Grazie dal profondo del mio cuore. E vorrei anche ringraziare i miei nonni, supporto indispensabile per la mia crescita, e i miei zii, in particolare zio Francesco, sempre disponibile a darmi un passaggio per Bari al momento delle partenze, e allo stesso modo, per venire a prendermi al momento del ritorno.



# Abstract

The present study aims to investigate and analyze the combustion process in a squared single-element combustion chamber using gaseous oxygen/gaseous hydrogen as propellant mixture. Propellants are injected at ambient temperature with a shear coaxial injector. All investigations, in particular flame emission, flame structure and its anchoring, are studied through a non-invasive optical diagnostic method, using an optically accessible combustion chamber operated at 20 and 10 bar pressure level. A digital camera was used to detect the flame anchoring near the oxygen post tip. On the other hand, to characterize the flame front and combustion process at different ROFs, the detection of hydroxyl radicals emission was performed. Flame emission, based on the chemiluminescence theory, was detected using the iCCD Camera FlameStar 2 equipped with a filter, able to record light emitted from the thermally or chemically excited OH, denoted OH\*, when they naturally return to ground state OH. Moreover, the images obtained were corrected through a matlab script able to apply shading correction; the needs and the theory behind the developed code will be presented in order to have a clear vision on the usefulness of this correction.



# Contents

<b>1</b>	<b>Introduction</b>	<b>1</b>
1.1	Design of a rocket: the choice of propellant . . . . .	1
1.2	Chemiluminescence Review . . . . .	2
1.2.1	Flame Spectrum . . . . .	3
1.2.2	OH* Emission . . . . .	5
1.2.3	The Blue Radiation . . . . .	6
1.3	Optical diagnostic for combustion . . . . .	8
<b>2</b>	<b>Hardware and Experimental Setup</b>	<b>12</b>
2.1	Hardware Description . . . . .	12
2.2	Operating Conditions And Sequence . . . . .	16
2.3	Optical Setup and Diagnostics . . . . .	17
<b>3</b>	<b>Image Post-processing</b>	<b>20</b>
3.1	Image Post-processing Steps . . . . .	20
3.1.1	Angle Correction . . . . .	21
3.1.2	Image Resizing . . . . .	21
3.1.3	Average . . . . .	22
3.1.4	Shading Correction . . . . .	22
<b>4</b>	<b>Operative Conditions and Test Results</b>	<b>32</b>
4.1	Pressure Distribution along Chamber Axis . . . . .	36
4.1.1	Film Cooling Analysis . . . . .	39
4.2	Temperature Distribution . . . . .	40
4.2.1	Temperature Distribution along Chamber Axis . . . . .	40
4.2.2	Temperature Distribution along Time . . . . .	41
4.2.3	Film Cooling Analysis . . . . .	43
4.3	Combustion Efficiency . . . . .	45
4.3.1	Film Cooling Analysis . . . . .	47

---

<b>5</b>	<b>Imaging Results and Discussion</b>	<b>48</b>
5.1	Flame Anchoring and Stabilization . . . . .	48
5.2	OH* Emission . . . . .	52
<b>6</b>	<b>Conclusions</b>	<b>58</b>
<b>A</b>	<b>Matlab Code</b>	<b>64</b>
A.1	ICCD Camera . . . . .	64
A.2	Digital Camera . . . . .	69
<b>B</b>	<b>Experimental Data</b>	<b>73</b>
<b>C</b>	<b>Combustion Chamber Photos</b>	<b>75</b>

# List of Figures

1.1	Hydrogen storage tank . . . . .	2
1.2	Typical chemiluminescence spectrum of an atmospheric hydrogen-air flame.	5
1.3	Spectrum of the flame 5 mm above the fuel lance at different pressures. . .	8
2.1	Combustion chamber setup . . . . .	13
2.2	Injector configuration . . . . .	13
2.3	Single shear coaxial injector element . . . . .	14
2.4	Thermocouples configuration along the combustion chamber axis . . . . .	15
2.5	Test nominal load points . . . . .	16
2.6	FlameStar 2 system . . . . .	18
2.7	Optical setup for both cameras . . . . .	19
3.1	Macro image (a) with nonuniform illumination. The background image (b) was recorded under the same conditions. Dividing or Subtracting the background image pixel by pixel into the original, is produces a leveled image (c) . . . . .	23
3.2	Figure 3.2a ( $\sigma = 1$ ) is compared to Figure 3.2b in which the standard deviation has a higher value ( $\sigma = 3$ ) . . . . .	25
3.3	On the left there is the original calibration image, in case of $P_c = 10$ bar e $OF = 4.4$ , while on the right there is the corresponding background with $\sigma = 10$ . . . . .	26
3.4	On the left there is the corresponding image resulting from the subtraction with background with $\sigma = 10$ , while on the right there is the corresponding image with shading correction . . . . .	26
3.5	On the left is shown the brightness of original image along x; on the right there is the brightness graph of corrected image . . . . .	27
3.6	On the left there is the original flame image, in case of $P_c = 10$ bar e $OF = 4.4$ , on the right there is the corresponding background with $\sigma = 10$ , while below is shown the corresponding image with shading correction . . . . .	28

---

3.7	The image at the top left shows the original calibration image; the image at the top right shows the background constructed starting from a Gaussian filter with $\sigma = 10$ ; the photo below shows the corrected calibration image . . . . .	29
3.8	On the left is shown the brightness of original image along x; on the right there is the brightness graph of corresponding corrected image . . . . .	29
3.9	On the left there is the original flame image, in case of $P_c = 20$ bar e $OF = 6.0$ , while on the right there is the corresponding image with shading correction . . . . .	29
3.10	On the left there is the original calibration image, in case of $P_c = 20$ bar e $OF = 4.4$ , while on the right there is the corresponding background with $\sigma = 10$ . . . . .	30
3.11	On the left there is the corresponding image resulting from the division with background with $\sigma = 10$ (3.10), while on the right there is the corresponding image with shading correction . . . . .	30
3.12	On the left is shown the brightness of original image along x; on the right there is the brightness graph of corrected image . . . . .	31
3.13	On the left there is the original flame image, in case of $P_c = 20$ bar e $OF = 4.4$ , on the right there is the corresponding background with $\sigma = 10$ , while below is shown the corresponding image with shading correction . . . . .	31
4.1	Nominal load points with error bar . . . . .	33
4.2	Some examples of mixture ratio trends in time . . . . .	34
4.3	Velocity Ratio and Momentum Flux Ratio at different load points . . . . .	35
4.4	Normalized pressure (respect to $p_{me}$ ) distribution along combustion chamber axis . . . . .	36
4.5	Trend in pressures, during the combustion time, detected by the nine probes along the axis of the combustion chamber . . . . .	38
4.6	Pressure distribution along combustion chamber axis . . . . .	39
4.7	Temperature distribution along combustion chamber axis . . . . .	40
4.8	Temperature profiles for 10 bar cases, during combustion time, detected by the nine probes along the lower side of the combustion chamber longer segment . . . . .	41
4.9	Temperature profiles for 20 bar cases, during combustion time, detected by the nine probes along the lower side of the combustion chamber longer segment . . . . .	42
4.10	Temperature distribution along combustion chamber axis . . . . .	43

---

4.11	Trend in temperature, during combustion time, detected by the nine probes along the lower side of the combustion chamber longer segment . . . . .	44
4.12	Combustion efficiency values for each load points . . . . .	46
4.13	Comparison between combustion efficiency values . . . . .	47
5.1	Start Up and Flame Anchoring for 20 bar and OF = 4.4 case . . . . .	49
5.2	Start Up and Flame Anchoring comparison for 20 bar and OF = 4.4 case, without Film Cooling . . . . .	50
5.3	ShutDown for 20 bar and OF = 4.4 case . . . . .	51
5.4	ShutDown comparison for 20 bar and OF = 4.4 case, without Film Cooling	51
5.5	OH* Emission images for each load point at a chamber pressure of 10 bar .	52
5.6	OH* Emission images for each load point at a chamber pressure of 20 bar .	52
5.7	OH* Emission trends at different axial distances and a chamber pressure of 10 bar . . . . .	53
5.8	OH* Emission trends at different axial distances and a chamber pressure of 20 bar . . . . .	54
5.9	OH* Emission trends along horizontal main axes at a chamber pressure of 10 bar . . . . .	56
5.10	OH* Emission trends along horizontal main axes at a chamber pressure of 20 bar . . . . .	57
C.1	Camera optical bench . . . . .	75
C.2	Optical access to combustion chamber . . . . .	76
C.3	Insertion of the quartz window into the appropriate cavity . . . . .	77
C.4	Frontal view of MoRaP . . . . .	78
C.5	MoRaP . . . . .	79
C.6	Combustion chamber during experiment . . . . .	80

# List of Tables

2.1	Combustion chamber geometry . . . . .	12
2.2	Injector geometry . . . . .	14
4.1	Test nominal points . . . . .	32

# Nomenclature

## List of Symbols and Variables

$A$	[m <sup>2</sup> ]	Cross Section Area
$t$	[m]	Post Wall Thickness
$z$	[m]	Axial Coordinate Along the Combustion Chamber
$\sigma$	[–]	Standard Deviation
$P_{cc}$	[bar]	Combustion Chamber Pressure
$J$	[–]	Fuel to Oxidizer Momentum Flux Ratio
$VR$	[–]	Fuel to Oxidizer Velocity Ratio
$\rho$	[Kg/m <sup>3</sup> ]	Static Density
$P$	[bar]	Static Pressure
$P_{tot}$	[bar]	Total Pressure
$T$	[K]	Static Temperature
$R$	[m <sup>3</sup> Pa/Kmol]	Gas Perfect Costant
$\lambda$	[–]	Specific Heat ratio
$M_m$	[Kg/mol]	Molar Mass
$\dot{m}$	[Kg/s]	Mass Flow Rate
$u$	[m/s]	Flow Stream Axial Velocity
$\dot{q}$	[W/m <sup>2</sup> ]	Heat Flux
$c^*$	[m/s]	Characteristic Exhaust Velocity
$c_{exp}^*$	[m/s]	Experimental Characteristic Velocity
$c_{theo}^*$	[m/s]	Theoretical Characteristic Velocity
$\eta_{c^*}$	[–]	Combustion Efficiency

## Abbreviations

TUM	Technische Universität München
ROF	Oxygen to Fuel Ratio
OF	Oxygen to Fuel
GOX	Gaseous Oxygen
GH <sub>2</sub>	Gaseous Hydrogen
LOX	Liquid Oxygen
LH <sub>2</sub>	Liquid Hydrogen
GCH <sub>4</sub>	Gaseous Methane
GN <sub>2</sub>	Gaseous Nitrogen
MoRaP	Mobile Rocket Combustion Chamber Test Bench
CMOS	Complementary metal-oxide semiconductor
OH	Hydroxyl Radicals ground state
OH*	Hydroxyl Radicals excited
CEA	Chemical Equilibrium with Applications
LPF	Low Pass Filter

# Chapter 1

## Introduction

### 1.1 Design of a rocket: the choice of propellant

In a design process for a rocket engine it is fundamental the choice of propellant. There are four main types of chemical rocket propellants: solid, storable liquid, cryogenic liquid and liquid monopropellant. Usually the choice of the consistency of the fuel / oxidizer determines the functioning of the engine itself. The most common rocket categories are basically two: liquid or solid rockets. However, a third category has been developed and it has gained attention for the future: hybrid engines consist of a liquid oxidizer reacted with a solid fuel.[24]. For each of these categories there are advantages and disadvantages. Solid fuels can provide huge amounts of thrust, and is often used as a booster making a satellite launching rocket gain high initial velocity before using higher-efficient liquid motors to gain horizontal velocity above the thickest part of the atmosphere. They are much easier to store and handle so another advantage is that a solid rocket is very simple. On the other hand it can never be switched off by command and can not be throttled as a liquid or hybrid motor can. It is usually less efficient than liquid motors.

The other possible choice is a liquid fuel/oxidizer mixture. There are several advantages for this category: the energy density tends to be higher than solid fuels and this leads to a higher combustion temperature. Therefore the specific impulse (impulse [in Newton seconds] per kilogram of propellant) is very large. Another advantage is that the thrust can be controlled (throttled) and that the engines can even be shut down and re started at a later flight stage. The biggest disadvantage of liquid fuels is the necessity for pumps, piping and separate storage (Fig.1.1) for the fuel and oxidant; this means that extra mass has to be carried by the launch vehicle.

Finally, the last category is that of hybrid solid/liquid bi-propellant rockets. They have higher specific impulse than solid state motors, but is throttleable and can be shut down as liquid motors can. The biggest problem of hybrid motors is that they have a low thrust



**Figure 1.1:** Hydrogen storage tank

compared to the total impulse. They are considered very safe since the fuel and oxidizer can be stored and shipped individually, and each component is by itself completely safe. However, the focus in this study will be on liquid propulsion.

Between all liquid fuels the most commonly used is liquid hydrogen. Hydrogen has the lowest molecular weight of any known substance and burns with extreme intensity in combination with an oxidizer such as liquid oxygen (temperature of nearly 3,000 K[5]). Liquid hydrogen yields the highest specific impulse, or efficiency in relation to the amount of propellant consumed, of any known rocket propellant. Because liquid oxygen and liquid hydrogen are both cryogenic – gases that can be liquefied only at extremely low temperatures – they pose enormous technical challenges with high operational and handling costs and a very high degree of danger[25].

This, together with other motivations, has led to increasing attention to hydrocarbons as a propellant for future launch vehicles. In this context oxygen/methane is one of the most promising propellant combinations. Unfortunately the amount of experimental test data is still low to develop a new rocket engine using this propellant combination; thus the comparison with a more mature technology like LOX/LH<sub>2</sub> is necessary.

## 1.2 Chemiluminescence Review

The study of combustion process is usually carried out with the measurement of the heat release. This operation contains however some difficulties of technical nature. Therefore, the heat release rate is measured indirectly in most applications. A common quantity for such indirect measurements, made by non-invasive optical means, is the light emission of the flame. Before explaining how the light emission is linked to the measurement of heat release rate, it will be useful to give a general theoretical background on the flame radiation. A more complete discussion can be found in the Phd thesis of Thomas Fiala[6] and Lauer[19], from which inspiration was taken to explain and summarize this subtopic.

### 1.2.1 Flame Spectrum

Flames can be characterized by their emission or absorption spectrum. These are defined by the distributions of the emitted or absorbed radiance as a function of wavelength  $\lambda$ . In order to better understand how a flame spectrum is developed, it will be essential to not consider the radiation as a wave but as a particle phenomena. As Fiala says in [6]: "For quantum theory each single wavelength can be attributed to a stream of photons, each having the corresponding energy showed in equation (1.1). A regular (un-ionized and non-dissociated) molecule or atom can only occupy discrete energy states. Each state is characterized by its electronic, vibrational, rotational, and spin quantum numbers. A molecule can transit from a higher energy state  $i$  to a lower energy state  $j$  spontaneously, if it is not forbidden by the selection rules of quantum mechanics. The probability occurring that transition is known as the Einstein coefficient[23]. The Einstein coefficient is a constant for each transition and not a function of temperature or pressure."

$$E_{Photon} = h\nu = \frac{hc}{\lambda} \quad (1.1)$$

Displacement of a molecule from a higher energy (or ionized or dissociated) state to a lower energy state results in a emission of a photon. The energy difference  $\Delta E$  between the higher and lower states corresponds exactly to the energy  $E_{Photon}$  of the photon. The pure emission spectrum (without self-absorption) is defined by these Einstein coefficients and the number densities of the excited states. When thermal equilibrium is reached through collisions between molecules, that temperature defines density of the molecular states. It takes a different number of collisions to reach equilibrium, according to the states of the molecule (translational states, rotational states, vibrational states, electronic states[22]. At high temperatures and pressures, thermal equilibrium often is a good assumption.

Flames do not only emit radiation, but also can absorb it. The absorption spectrum is qualitatively similar to the emission spectrum for a single molecule. Photons can be absorbed by molecules only if they have the right value of energy to permit transitions between energy states (discrete levels). Molecules can absorb photons by raising its energy level with the energy of the photon. This is the inverse process of emission.

The overall observable spectrum of a flame generally is a function of both emission and absorption: The radiation emitted from excited molecules is subject to absorption by the same molecules present in the ground state. This process is known as self-absorption[1]. Self-absorption typically is significant for the radiation resulting from molecules substan-

tially present in flames and becomes more important with increasing pressure.

As Fiala suggest in [6]: "To investigate the origin of the radiation, it is therefore sufficient to clarify how the excited molecule  $M^*$  is being produced and how the chemical steady-state concentration is reached. As  $M^*$  is a sub-species of the ground species  $M$ , such an investigation is called detailed balancing . Generally, the excited species can be produced by three reactions:

1. Thermal collision with another molecule  $Q$ , there by transferring translational energy into excitation energy.
2. Absorption of a photon.
3. Chemical reaction of substances  $A$  and  $B$  forming the species  $M$  in the excited state. This reaction can also take place in presence of a third reactant.

All of the above reactions can also progress in the reverse direction, which deexcite the excited state. The reverse reaction of the thermal excitation is often referred to as *quenching*. The de-excitation process corresponding to the absorption reaction is essentially the spontaneous emission. The reverse of the chemical formation of the excited species  $M^*$  is a dissociation reaction."

Absorption and dissociation are commonly neglected because they always are much smaller than chemical and thermal excitation. In flames with temperatures above 2700 K, thermal excitation and quenching are the only remaining contributors to the population of  $M^*$  because they predominate over chemical excitation and spontaneous emission.  $M^*$  is in thermal equilibrium with  $M$ , and its concentration (and, therefore, its emission) is a function of the temperature and the ground state concentration  $M$  only([17][10]). In comparably cold flames (below 2500 K), radiation from excited molecules is observed which is much larger than the equilibrium radiation at that temperature. This is due to chemical excitation, and the resulting radiation is, therefore, called chemiluminescence.

*Chemiluminescence* is the phenomenon in which a chemical reaction leads to the emission of light, without incandescence, from atoms, molecules, or radicals , returning from an electronically excited state to ground state. Also in combustion processes there are chemical reaction and unstable energetic species[19]. When modeling chemiluminescence, both thermal excitation and absorption is often ignored and it is assumed that it is mainly influenced by the rate constant of the chemical excitation and the concentration of the reactants[26]. However, to correctly model chemiluminescence, also the reaction rates of the quenching reactions have to be known. Since chemiluminescence originates from the

reaction zone of the flame, it is commonly assumed to characterize the heat release rate of flame. In a hydrogen-oxygen flame there are only two dominant sources of radiation: the excited hydroxyl radical OH, which shows a typical band spectrum in the UV and a broad-band continuum in the visible, the blue radiation of hydrogen flames. There is also radiation originating from vibrational excitation of water vapor and OH in the near infra-red, even if this is a process less important. However, the measurement of flame radiation has several disadvantages: measurements based on optical measurements are always subject to positioning errors and are also influenced by external factors such as ambient light and camera quality. It means that a complicated post-processing of image is required. Second and more important, radiation is a quantity not directly associated with a single thermodynamic property. This lead to a great possibility of interpretation[6].

### 1.2.2 OH\* Emission

The radiation from the excited hydroxyl radical OH\* is the most distinct radiation of flames and is found in the combustion of all fuels containing hydrogen(Fig.1.2). A comprehensive summary on the OH\* radiation from flames is given by Gaydon[8] or Mavrodineanu and Boiteux[22]. The chemical reactions probable to form OH\* in the excited state have

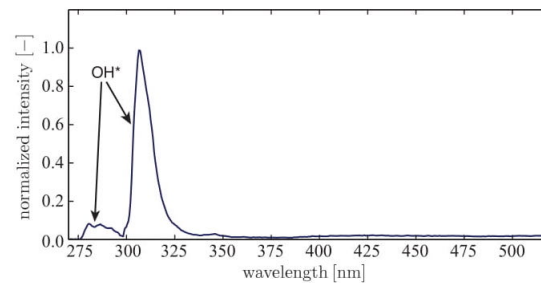


**Figure 1.2:** Typical chemiluminescence spectrum of an atmospheric hydrogen-air flame.

been investigated in many studies([13][18][15][20][12]). For hydrogen flames, most authors came to the conclusion that the dominant reaction is:



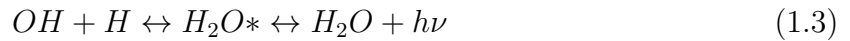
The great part of OH\* radiation are in UV band, specifically about a length wave of 306.4 nm. To determinate the spectral properties of OH, it was necessary and it is still necessary to perform many experimental tests because the results are variable depending on the experimental test itself and the measurement and environmental conditions in which it is conducted. Through the numerous tests carried out in the past it was possible to create

a database in which the experimental einstein coefficients have been inserted. For certain conditions, which coincide with those of the tests recorded, it is possible to consult this database. It is still important to analyze the behavior of OH\* chemiluminescence to look for a relationship with environmental factors, such as pressure. Gaydon and co-workers found an abnormality in low-pressure hydrogen-air flames([10][8][9]). The results found varied greatly from what was theoretically expected. This fundamentally could be due to two reasons: reaction mechanisms not modeled well and neglecting of self-absorption. Even at high pressures, the behavior of the OH\* radiation is ambiguous. Higher intensities of radiation would be expected at higher pressures, due to the fact that the adiabatic temperature of the flame is higher. This trend has early been confirmed by Liveing and Dewar[21]. They found out that the radiation intensity of a nonpremixed oxygen-in-hydrogen flame increased with approximately  $p^2$ , and that of a hydrogen-in-oxygen flame with a slightly smaller exponent. On the other hand, Klimenko et al.[16] measured a different trend in a very similar combustion chamber: At two different locations, OH\* radiation remained constant or even decreased for an increase in pressure. They estimated that this effect is due to recirculated products around the flame absorbing radiation. Higgins et al.[14] reported the intensity of OH\* radiation in a premixed methane flame to be proportional to  $p^{-0.86}$ , thus decreasing. This summary shows that the pressure influence on the OH\* radiation cannot be trivially described, but varies strongly depending on the test and measurement conditions.

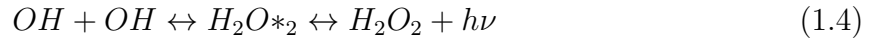
### 1.2.3 The Blue Radiation

The blue radiation is the most distinct radiation of hydrogen flames visible to the human eye. Hydrogen flames emits this broadband radiation spectrum which peaks at approximately 440 nm. The spectrum shows a continuous shape with a superimposed fine structure. It extends from 220 nm to about 600 nm, showing a flat maximum at 440 nm. It is thereby sometimes also referred to as blue radiation. The theory underlying the blue radiation is currently non-existent, so it is necessary to rely on theoretical suppositions to be tested experimentally. For example, the origin of blue radiation is not yet clear. Gaydon[8] summarized three possible sources: It could be 1) an unresolved structure of the OH bands, 2) radiation from ionisable impurities (which was formerly also proposed by Finkelnburg[7]), or 3) a chemiluminescent reaction. Of these three options Diederichsen and Wolfhard[3] and Schefer et al.[30] managed to exclude the first two. This leaves a chemiluminescent reaction as the only possibility. Gaydon[10] proposed the following

reaction forming water vapor:



In addition, Diederichsen and Wolfhard[3] suggested a reaction forming hydrogen peroxide, which was in slightly better agreement with their observed pressure dependency:



Both reactions were studied by Padley[27] and Vanpee and Mainiero[32] and an excellent summary, of how the study was conducted and of the conclusions to which it led, is included in the paper of T. Fiala and T. Sattelmayer. Padley recorded the total emission of a non-premixed hydrogen-oxygen flame diluted with nitrogen. By varying the nitrogen content, he was able to control the flame temperature. His comparison of equilibrium radical concentrations with the recorded intensity yielded a better description by first equation. In contrast, Vanpee and Mainiero came to the opposite conclusion. They studied the radiation from argon-diluted non-premixed hydrogen-oxygen flames, premixed hydrogen-oxygen flames, and premixed hydrogen-nitric oxide flames, each at varying equivalence ratios. Their comparison with equilibrium radical concentrations showed a better agreement with second equation. A laminar hydrogen-oxygen flame is studied both experimentally and numerically at different pressures. From the experiment, the actual radiation can be measured. A numerical simulation featuring detailed chemistry provides the spatial concentrations of OH and H as well as the temperature. The validation of the simulation is achieved by comparing the measured and simulated OH\* radiation.

Experimentally it has been seen that this radiation is weak in cold and low-pressure flames (Frankland in 1867). As it is possible to observe in the experimental flame spectrum (fig.1.3), at elevated pressures and high temperatures, it can contribute significantly to the overall emission. The continuous spectrum exhibits the features known from literature. The flat maximum lies at approximately 440 nm. The radiation intensity increases with pressure for both the OH\* emission and the blue emission. For OH\*, the pressure influence appears to be less significant at elevated levels. The peak appears to become sharper with rising pressure and temperature. Apart from the OH bands, no superimposed radiation is observed. Therefore, it can be concluded that the signal recorded around 456 nm is attributed purely to the blue continuous radiation. To further study the blue radiation, the band-pass filtered radiation around 456 nm is examined in detail. No sign of self-absorption is observed for this radiation. For a broad range of pressures, the radiation is recorded. The experimental data is compared to the proposed models both spatially for

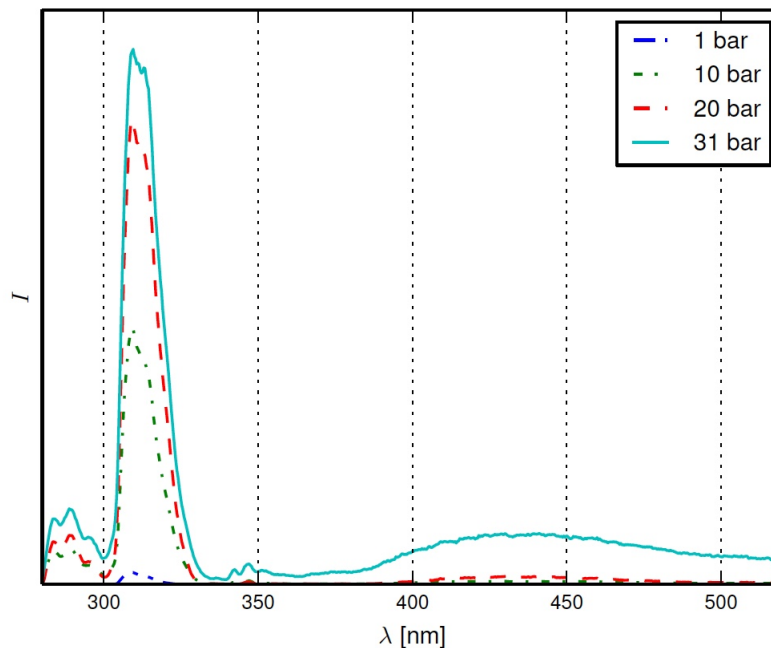


**Figure 1.3:** Spectrum of the flame 5 mm above the fuel lance at different pressures.

individual pressures and by the total radiation as a function of pressure. In both cases, the chemiluminescence model forming  $H_2O_2^*$  describes the experiment very well. The chemiluminescence model forming  $H_2O^*$  under-predicts the pressure influence if the Arrhenius and quenching parameters are set to zero. It further suggests a flame thicker and longer than observed in the experiment. The results show that the blue continuous radiation can well be modeled by reaction forming  $H_2O_2^*$ . As the model predicts the radiation by taking the square of the concentration field of OH and self-absorption is not relevant, this provides a very simple and powerful tool to understand emission measurements and also to validate numerical simulations.

However, the low number of investigations and their partially contradicting results illustrate that the origin of the blue radiation is not yet fully clarified. Further research on this topic clearly is necessary to correctly understand the behavior of blue radiation.

### 1.3 Optical diagnostic for combustion

Optical diagnostics is a process of study and analysis, based on optical instruments, now suitable for many fields of scientific research. An example could be the microbiology in which the understanding of the behavior of living species is facilitated by the use of microscopes. Such behavior could not be perceived by man without the aid of optical

instruments capable of enhancing human analytical skills. Entering more specifically the case studied in this thesis, optical diagnostic techniques are commonly used in all kinds of fluid diagnostics, not only in combustion, but they are specially critical to flame diagnostics because of the hardship of the environment and small size.

Optical systems are ideal for combustion diagnostics because the non-invasive nature of these systems allows measurements to be taken without inserting a probe into the measurement region. Further combustion environments can be hostile and restrictive; hence optical techniques provide the benefit of accessibility and safety along with accurate results. To summarize, the positive aspects of optical diagnostic are manifold and can be listed in the following points:

1. Non-intrusive
2. Instantaneous with high spatial and temporal resolution
3. In-situ and real-time recording
4. 1D to 2D or 3D imaging
5. Modular and flexible system setups to expand capability by adding hardware for multi-parameter measurements

Optical techniques have some disadvantages, however. First of all, the radiation coming from the object may go through a complex path (windows, intermediate fluids, environmental air, and so on), with optical properties not well known or controllable; in fact one of the challenge with using these techniques on combustion chamber is providing suitable optical access. Second, the optical setups used to be most delicate and expensive. Third, when an optical diagnostic technique is used to study a phenomenon, the measurements will be performed at different times. Due to the nature of the diagnostics, the measurements may not be carried out under the same conditions as the previous measurements. This is due to the fact that optical measurements are always subject to positioning errors and are also influenced by external factors . It will therefore be necessary to calibrate the equipment in the best possible way and with the same conditions as the previous tests. Fourth, good post-processing work is needed.

As we have already mentioned, during the combustion process, the many reactions that occur in the flame front create a region of high local heat release. Thus, a great deal of combustion research focuses on this flame region. Since the flame front itself may not be possible to monitor, experimental investigations of this region have aimed at studying some other closely related property. One important intermediate species in the oxidation of fuels is the OH radical. Because it is formed in the flame front, OH is a commonly used

marker for this region. In the first analysis, a division of optical diagnostic techniques can be between active and passive techniques. Active techniques detect the fluorescence signals emitted when OH radicals excited by a high-energy laser beam return to their ground state. These techniques are named with the acronym LIF, that is laser-induced fluorescence. To measure flame shapes in two dimensions are readily available the planar laser-induced fluorescence (PLIF). In PLIF, a pulsed wavelength tuneable laser source forms a thin sheet of light, which criss-crosses the flow field (flame area) under study. When the laser wavelength is resonant with an optical transition of a species (chemical ion or molecule) in the flow, a fraction of the incident light will be absorbed at points within the illumination plane. Some of the absorbed photons are subsequently re-emitted with a new spectral distribution, which is different for each molecule/species and also varies with the local flow field conditions in the flame. Fluorescence is produced by the excitation of species such as OH in the flame by a pumped dye laser. The emitted fluorescence is collected and imaged onto a solid-state array camera, which is typically coupled to a image-intensifier to provide snapshots of the fast flows with improved sensitivity, as the intensity of species of interest emitted fluorescence can be extremely low. The amount of light (fluorescence) detected by pixels in the camera depends on the concentration of the species being studied within the measurement zone of the flame and the local flow field conditions, i.e., temperature, pressure and mixture composition. Extending these measurements to three dimensions requires additional laser sheets and multiple cameras, which increases the cost and complexity significantly. Another technique based on laser is the Particle Image Velocimetry (PIV). PIV is a laser-based optical technique for the characterization of flow and turbulence dynamics in combustion processes. Typical PIV measurements use dual laser pulses to probe the flow field and determine the two velocity components of features of interest in a single plane simultaneously. However, these laser-based techniques have some drawbacks: Data collection and processing in these systems is also complex, which reduces the flexibility of the measurements and requires expert users. Laser measurements require optical access in two or more directions, which inhibits their application in practical burners that are typically enclosed and require special optical access to be installed. Thus, there is a need to develop optical diagnostic techniques that collect similarly useful data but with lower cost, less complexity, and limited optical access, allowing measurements to be taken more easily. And it is for these negative aspects that it is preferred, in certain cases, to choose less expensive and complex techniques.

Flame shapes can be passively estimated from natural chemiluminescence without using a laser. In this case the camera records the light emitted from the chemically excited OH, denoted OH\*, when they naturally return to ground state. It is relatively easy to set up and useful to identify high-temperature reaction zones. This simpler approach has been

used successfully in many cases where the flame is two-dimensional or axisymmetric but it is limited to simple flame geometries and is generally difficult to interpret in turbulent flames, which often have features of interest in multiple planes. Emission imaging is also useful in situations where it is technically difficult or too costly to apply LIF such as optical engine diagnostics, where to follow single-cycle events it is preferred to acquire image data with high repetition rates. For true three-dimensional flame surfaces, Emission imaging typically only recovers the path integrated signal, and variations in the flame along the line of sight are not resolved. Just this last technique will be the one on which the whole flame analysis will be based in this study.

## Chapter 2

# Hardware and Experimental Setup

All experimental test campaigns presented in the following were performed at the Chair of Turbomachinery and Flight Propulsion's test facility at the Technical University of Munich (TUM). The mobile test rig (Mobile Rocket Combustion Chamber Test Bench, MoRaP) is operated with gaseous oxygen-gaseous hydrogen (GOX/GH<sub>2</sub>), designed for nominal interface pressures up to 50 bar, allowing variations in combustion chamber inner cross section, length and injector configuration. In this chapter the whole experimental apparatus will be described. Firstly, the characteristics of the combustion chamber used for the experiment will be illustrated; secondly a description about injector geometry will be given and finally a summary of the flow conditions and data analysis procedures will be presented. Furthermore, the optical setup used will also be explained in detail to better understand the flame detection process.

### 2.1 Hardware Description

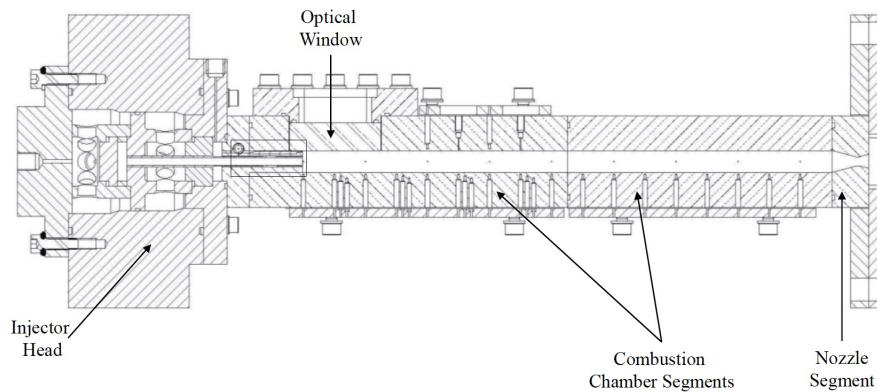
The investigation presented are performed using a modular capacitive cooled combustion chamber with a square cross section of 12 mm x 12 mm (Tab. 2.1).

Length	290	[mm]
Width	12	[mm]
Height	12	[mm]
Throat height	4.8	[mm]
Contraction Ratio	2.5	[-]

**Table 2.1:** Combustion chamber geometry

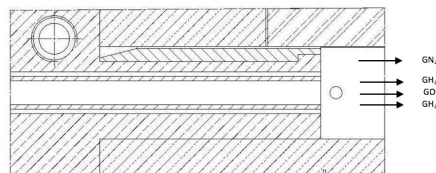
The material selected for the combustion chamber and nozzle segments is oxygen-free copper (Cu-HCP) due to its high thermal conductivity. In addition to a higher ther-

mal conductivity, the oxygen-free copper has an excellent corrosion resistance and a good electrical conductivity, which permits an higher energy transfer. Other important characteristics of this material are: the resistance to hydrogen embrittlement, an excellent formability, a good weldability. Because of the material used, the pressure, the OF ratio and the burning times must be contained. Thus the combustion chamber is designed for a testing time of up to 2 s at a maximum chamber pressure of 20 bar. The maximum reachable value of OF ratio is 6.8, just for hydrogen-oxygen flame at 10 bar. This chamber has already been described in detail by previous papers from Celano et al [2]. The single-element rocket combustion chamber, depicted in Figure 2.1, consists of an injector head, two chamber segments and a nozzle segment.



**Figure 2.1:** Combustion chamber setup

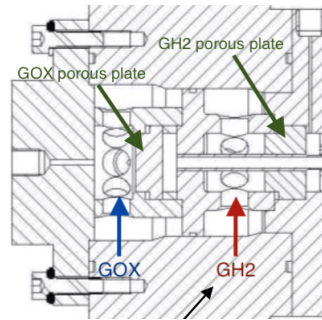
The injector head of the combustor allows the use of different injector designs. For the current study, a single shear coaxial injector element is integrated as shown in Fig. 2.2. The main geometric characteristics of injector are illustrated in table 2.2.



**Figure 2.2:** Injector configuration

To ensure homogeneous injection conditions, in terms of temperature and pressure, two porous plates are placed in the oxidizer and fuel manifolds respectively (Fig. 2.3). The nozzle segment is 20 mm long and differs from a usual configuration due to its rectangular throat cross section of 4.8 mm x 12 mm. A Mach number of 0.24, typical for rocket

GOX inner diameter	4	[mm]
GOX post wall thickness	0.5	[mm]
GH2 external diameter	6	[mm]
Injector area Ratio	0.7	[-]

**Table 2.2:** Injector geometry**Figure 2.3:** Single shear coaxial injector element

applications, is achieved with a contraction ratio of 2.5.

The combustion chamber is equipped with equally spaced pressure transducers and thermocouples type T mounted in the wall along the chamber axis to characterize the combustion process and to monitor heat release (Fig. 2.4). As already described in detail by Celano et al. [2], nine equally spaced - 34 mm - pressure transducers WIKA A10 placed on the side of the combustion chamber (PC0,...,PC8) allow for evaluation of the pressure distribution along the combustor axis,  $p(z)$ , the first pressure transducer (PC0) being positioned 0.5 mm away from the injector face-plate. All the pressure transducers are individually calibrated and operated at a data acquisition rate of 100 Hz. Furthermore to characterize the injection conditions, thermocouples of Type K, with 0.5 mm diameter, and a pressure transducer, are installed in the injector manifolds, prior the porous plates. To determine, instead, the temperature field within the chamber material, clusters of Type T thermocouples of 0.5 mm diameter are located at different distances (1, 2 and 3 mm) from the hot gas wall. The Type T thermocouples are mounted with a regular path of 17 mm, with the first at 0.5 mm from faceplate, in the down surface of the first and second segment, along the center plane of the combustion chamber. Two Medtherm coaxial type T thermocouples are positioned on the top of the combustion chamber first segment, flush mounted with the wall, while five type K surface thermocouples are placed to its external surface. A spring loaded system ensures contact between type T thermocouple tips and the base of the housing holes, providing a constant force of about 2 N, thus minimising the chance of potential loss of contact because of vibrations or material expansion/contraction

during hot firing tests. Medtherm thermocouples are press-fitted into the chamber wall. In order to ensure better contact, the tip has been polished to match the flat surface of the chamber. The thermocouple location pattern is shown in Figure 2.4.

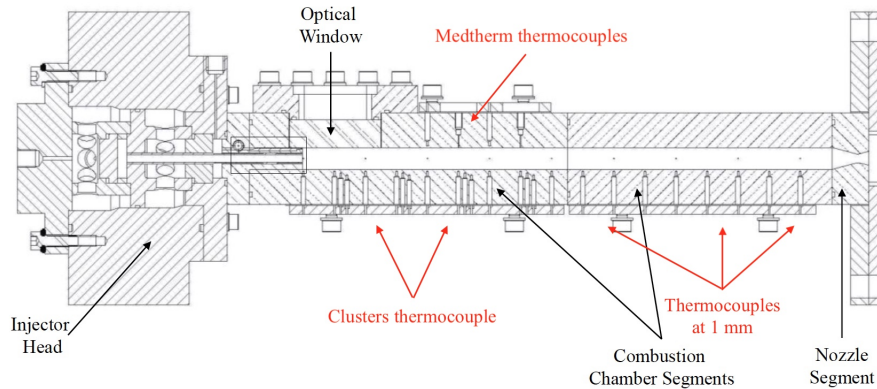


**Figure 2.4:** Thermocouples configuration along the combustion chamber axis

The optical access to the flame is possible through a rectangular flat window, made of quartz, placed on the upper part of the combustion chamber (Fig.2.1). When a flat window is applied to a round combustion chamber, flow disturbance phenomena arise, caused by the presence of the window corners. These disturbances are precisely avoided by the configuration used in this case, that is, a flat window applied to a square combustion chamber.

The quartz window has few tenths of a millimeter from the surrounding walls in the rectangular space, where it must be placed. To prevent the mechanical shock from breaking the delicate quartz window, very thin sheets of graphite have been placed on all four sides. The graphite sheets have the task of filling the spaces of tolerance and therefore keeping the window firmly in place, and also to soften the shocks, thanks to the excellent elastic properties of the graphite.

A film cooling of gaseous nitrogen is used, as coolant, to protect the quartz window from high temperatures in the combustion chamber and therefore from the high thermal fluxes from inside to outside. In order not to influence the near-injector flame stabilization an inert gas is required; for this reason the gaseous nitrogen (GN<sub>2</sub>) was chosen. Furthermore, to ensure the least possible impact, a small percentage of nitrogen was used compared to the total mass of the flow.

## 2.2 Operating Conditions And Sequence

For determination of the load points, the characteristic velocity is calculated with the software tool NASA CEA2 and combustion efficiency is assumed to be equal to 1. Figure ?? summarizes the chosen nominal load points.

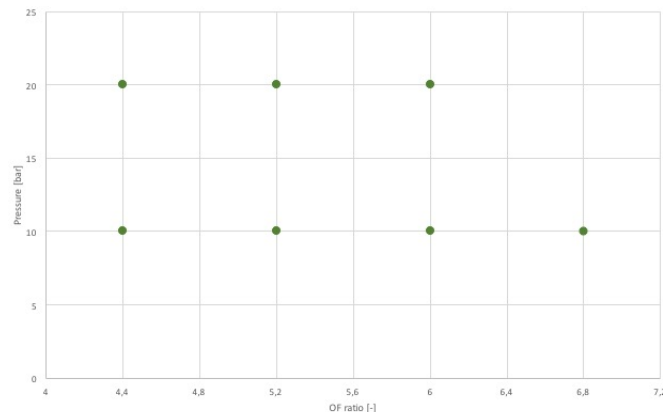


**Figure 2.5:** Test nominal load points

First of all the combustion chamber was cleaned up from possible slag from previous experiments. The waste was thrown out through the purge gas operated by the graphical interface in LabVIEW. Through this graphical interface it is possible to control the combustion chamber in all its aspects, to vary operating conditions and to change the test sequences. For example, always thanks to the graphic software, propellants, purge gas, and film cooling mass flow rates can be adjusted by adapting the upstream pressure of sonic measuring orifices located in the feedlines. Afterwards the quartz window was cleaned with ethanol and after that it was housed in the rectangular space on the upper face of the chamber, together with the graphite sheets, as mentioned in the previous paragraph. After the hydrogen, oxygen and nitrogen tanks were safely and connected to the test bench, the absence of leaks in the combustion chamber was verified. The combustion chamber was closed and filled with purge; the pressure was monitored and if a pressure drop was detected, leaking source was search and the process repeated. In most cases the cause was due to an incorrect positioning of the quartz window and the graphite sheets. The optimal position of the window was therefore found, when the pressure in the combustion chamber was constant. A check was also made of the correct functioning of the thermocouples simply by observing in labview the temperatures reached by the thermocouples along the axis of the chamber. So at first it was ensured that the tests were carried out correctly, making sure that all the equipment worked as well as possible. After having arranged the optical instrumentation, better explained in the following paragraph, the sequence can

be started through the control software. The sequence is divided into three main periods: transient start-up with ignition, main combustion chamber operation and shut down. The igniter operates for 300 ms to ensure ignition of the combustion chamber for a total burning time of 2 s. A spark torch igniter is used to ignite the propellant mixture. The igniter operates with gaseous hydrogen and oxygen and is located in the middle of the combustion chamber with respect to the axial direction. After successful ignition of the main combustion chamber the igniter is switched off. The same sequence is applied to all of the tests performed. As it is possible to notice in the Figure 2.5, all tests conducted will be at 10 and 20 bar. For each of the two levels of pressure in the combustion chamber, cases will be analyzed with a ROF ranging from 4.4 to 6 (6.8 only in the case of pressure of 10 bar) and a percentage of film cooling of 20%. Mixture ratio (ROF) or oxygen to fuel ratio is defined as the ratio between mass flow rate of oxygen and fuel (Eq. 2.1).

$$OF = \frac{\dot{m}_{GOX}}{\dot{m}_{GH_2}} \quad (2.1)$$

Each of the cases analyzed (which in total will be 14) will be observed with both cameras available. It will be used a digital camera to observe the flame anchoring and subsequent stabilization and a iCCD Camera will be used to detect OH radical emissions, thanks to a filter placed in front of the lens. Additionally, through the digital camera two extra cases will be analyzed: at 20 bar with a ROF of 6.8 and 4.4, without film cooling, in order to study the influence of the film cooling on the flame shape stabilization.

## 2.3 Optical Setup and Diagnostics

The monochromatic Digital Camera from Toshiba (USB Camera) was used to capture the start-up and flame anchoring process. The complete optical accessible area is visualized with a resolution of 2048 x 1088 pixels and a frame rate up to 168 fps. During the tests the following parameters were set: exposure time of 50  $\mu$ s, and aperture of 6. This camera is controlled by a PC and the system is simple compared to that of the ICCD camera. In fact, the small size camera is simply connected, via USB, to the PC control unit, and directly from the PC it is activated and parameters are configured.

On the other hand, to detect spontaneous emission of intermittently existing hydroxyl (OH\*) radicals, a different camera was selected to record the tests: iCCD Camera FlameStar 2, filtered, with a resolution of 384x287 pixels and a frame rate of 4 fps. During the tests the following parameters were set: exposure time of 5  $\mu$ s, gain equal to 10 and aperture of 22. This camera is controlled by a DaVis software PC, which allows us to set up

any technical parameter. On the whole functioning of this last camera there are other tools to consider, as can be seen in the Figure 2.6.

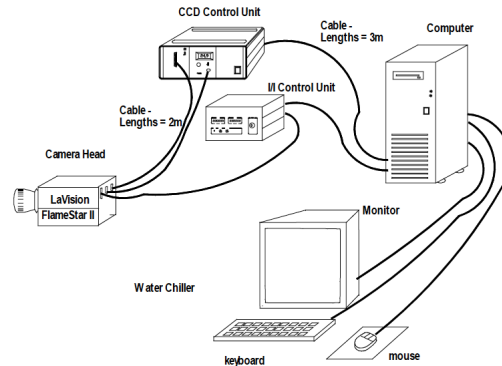


**Figure 2.6:** FlameStar 2 system

The whole system consists of:

1. *Camera Head*, that is the real optical sensor (CCD sensor), connected through optical fiber to an image intensifier (I/I).
2. *I/I control unit*, that operates the image intensifier; from this device it is possible to set the gain and the exposure time.
3. *CCD control unit (CCU)*, that operates the CCD sensor; therefore includes CCD electronics and thermoelectric stabilization (Peltier).
4. *Computer and monitor*, that control the whole system.

The operation of the whole system is explained shortly. When an image is acquired, the info is stored in the CCD of the camera head. All at the right temperature maintained by the Peltier stabilizer. The image is then read by the CCU. Within this the signal is converted into analog and transferred to an A/D converter in the PC. Here the signal is digitized and stored. These operations must be synchronized by an external clock or a computer. LaVision provides a TTL I/O board for the trigger.

After explaining in brief how the diagnostic system is made of, what features it is equipped with and how it works, it is possible to proceed with the logistic arrangement and the setting of the correct parameters. The flame detection arrangement is the same for both chambers. A metal support has been built on which both cameras were fixed. Then another support was placed in front of it, with a planar mirror positioned above the optical window with a 45-degree angle (Fig.2.7).

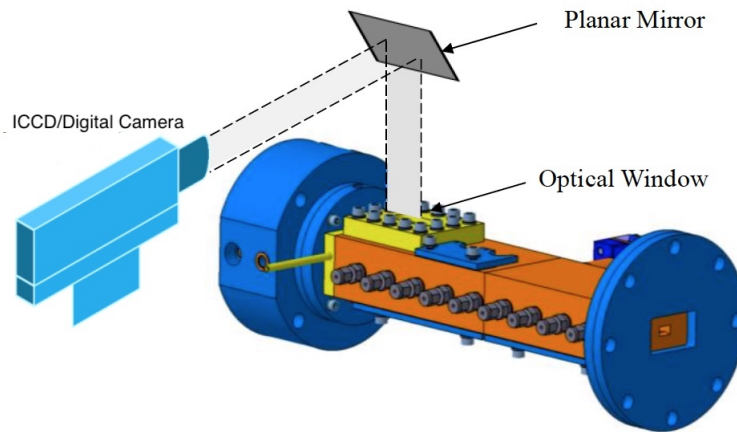


**Figure 2.7:** Optical setup for both cameras

This setup was chosen to protect the sensitive ICCD camera from possible damage. Both of them are substantially aligned in such a way as to have the same position for flame diagnostics. To calibrate both cameras and choose the best gain, focus and exposure values, a sheet of paper of the same size as the window from which you have visual access to the flame was used. On the sheet of paper were shown squares of size 2 mm, in a checkerboard motif. The exposure values were chosen based on the brightest flame, then on the case with chamber pressure of 20 bar and maximum ROF. The exposure value of the camera had to be such as not to have saturation in the image of the flame, and therefore loss of information. In this choice, also the right value of gain must be assessed; the values of these quantities had to be a compromise between the exposure time, the diaphragm opening and the gain. An exposure time that is too big, so too much light entering, and an excessively high gain leads to saturation. The focus was set through a graphic feedback, so the value was chosen for which the definition and the distinction was better, between the squares of the chessboard. Further photographic details can be found in the Appendix C.

## Chapter 3

# Image Post-processing

The optical diagnostics, as already mentioned in paragraph 1.3, by its nature is characterized by some disadvantages that make the post-processing of the image necessary. Making a post-processing of an image means improving the quality of information obtained from an image, without going to undermine or modify it. The objective pursued in this study will also be to create a Matlab code capable of post-processing the images collected by both cameras: iCCD FlameStar 2 Camera and the digital Camera. In collaboration with Pasquale, the prototype of a code was developed to correct areas of brightness inhomogeneity and average the instantaneous images, so as to have a single image to analyze for each test.

### 3.1 Image Post-processing Steps

The images collected by both cameras represent the flame at a precise instant of time. During the 2 second burning time, the iCCD camera will capture 8 images of the flame, while the digital camera more than a hundred, depending on the frame rate. Consecutive instantaneous images were averaged in the interval of stable combustion chamber operation. In this way it will be possible to eliminate the fluctuations of the flame present in the instantaneous image and to have an image that best represents the behavior of the flame in a continuous combustion time. But before doing this it will be appropriate to adjust the image in order to facilitate and make the calculation of the average more profitable. The first step will be an angular correction of the flame will be applied because it is inclined by a certain angle. This angle of inclination is an error due to the use of a 45 degree inclined mirror. Then a image's resizing in correspondence with the window will be applied, in such a way as to eliminate the influences of what is not strictly the flame in the process of calculating the average. So now it is possible to proceed with the average image process for the reasons already mentioned. Finally, however, a further

graphic correction must be applied. Due to internal irregularities of the camera lens, and due to variable ambient lighting, the captured photos will be characterized by a non-homogeneous background brightness. The result of this is that the information obtained contains inaccuracies. To solve this problem the so-called *Shading Correction* is applied to make the brightness homogeneous in the images and thus eliminate the differences in light due to the irregularities previously stated. It is important to keep the following 4 steps order in the post-processing actions of the image so as to have the results affected by errors as little as possible.

1. Angle correction;
2. Image resizing;
3. Average
4. Shading correction

In this thesis the step concerning shading correction will be detailed discussed. The other steps will be more detailed in the thesis of Pasquale Difficile. The correction processes is exactly the same for both cameras. So to summarize only the procedures applied to the Flamestar's pictures will be exposed.

### **3.1.1 Angle Correction**

As already mentioned, this topic will be examined in detail in the thesis of Pasquale Difficile [4]. The main objective is to correct a flame display error, which is inclined by a certain angle with respect to the imaginary horizontal axis of the picture. In this case, only the result obtained will be displayed in the following example.

### **3.1.2 Image Resizing**

The images captured by the iCCD FlameStar 2 camera will be eight for the two seconds of combustion established, but it will be considered only four photos (start up and shut down will be excluded). It was decided to work on a txt file uniquely associated with each photo. This txt file, automatically created by the camera represent the image in a single resolution. This is to facilitate management through Matlab code. The txt file of each photo will be read in the Matlab code and the matrix associated to the txt will be extracted. As a result, an array of numbers will be managed with dimensions equal to the resolution of the image, and each of them will represent a light intensity and therefore a color. So each number represents the color of a pixel. Previous each test the camera

is calibrated with a paper chessboard. The images of calibration are used as a reference for the window location when resized. This photo, depicting the optical access to the combustion chamber, will be taken before each test and is used to calibrate and properly focus the camera. It will be possible to trace the window position in terms of lengths along an x axis and a y axis. These references taken along the axes will correspond exactly to the pixel resolution of the cropped image. In practice, it will be known the initial and final matrix indices corresponding to the optical view field, and then it will be extrapolated a submatrix depicting only the window.

### 3.1.3 Average

The following paragraph presents only the graphic results obtained from the average process. The techniques used and the structure of the Matlab code will not be explained. Figures 3.3 and 3.6 show what has been obtained in the specific case of pressure 10 bar and  $OF = 4.4$ . For more information, it is advisable to refer to Pasquale Difficile's thesis [4] in which this image post-processing is explained.

### 3.1.4 Shading Correction

Shading correction will be the next step in the image post-processing steps. The approach used to solve the problem will be explained below only for the Flamestar camera's pictures. The same can be applied to the USB camera's picture and a small example will be given at the end of the paragraph.

The code part, attached in the appendix A, has been developed in a matlab environment and will have to interface with the code used to correct the other aspects listed above. The theoretical bases are not many but it is possible to arrive empirically to a solution. Naturally the code was based on existing theories in the field of image processing, theories summarized in the handbook by John C. Russ. As reported by John Rush in [29] "Given the diversity of image types and sources described above, there are several general criteria that can be prescribed for images intended for computer processing and analysis. The first is the need for global uniformity. The same type of object or structure should look the same wherever it appears in the image. This implies that brightness and color values should be the same and, consequently, that illumination must be uniform and stable for images acquired at different times."

The causes of an irregularity in the lighting uniformity can be multiple. When the viewing geometry is more complicated, either because the surface is not planar or the viewing angle is not perpendicular, the shades of colors and illumination can be affected and therefore

measurement is more difficult and requires geometric correction. Also the light source and the camera sensor, which capture the picture must be stable. It is easy for these devices to get out of perfect alignment and produce shading as well. Besides, lenses or cameras may cause vignetting, in which the corners of the image are darker than the center because the light is partially absorbed by greater path length in the optics and reduced by the change in the effective aperture of the lens. Also the environment, in which the test is held, may be characterized by an irregular light, coming from a single direction (for instance the sun) or not constant over time, which inevitably alters the perception of the phenomenon captured in photographs. Finally, bright specular reflections may cause saturation, blooming, or shifts in camera gain.

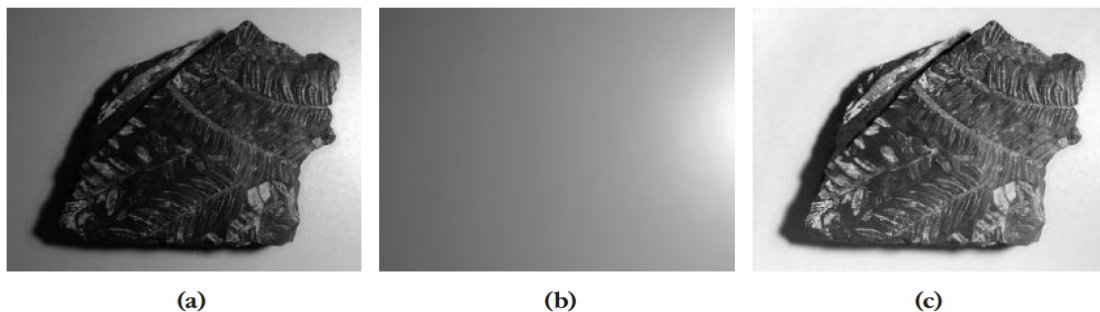


**Figure 3.1:** Macro image (a) with nonuniform illumination. The background image (b) was recorded under the same conditions. Dividing or Subtracting the background image pixel by pixel into the original, is produces a leveled image (c)

The example in Figure 3.1 shows an image with nonuniform illumination. Acquiring a "background" image by photographing the base of the copystand with no specimen present, but the same illumination, allows this nonuniformity to be leveled. The background image is either subtracted from or divided into the original, depending on whether the camera has a logarithmic or linear response. The difference is easily understood because in the linear case the corrected result is  $(Image)/(Background)$ , and when the signals are logarithmic, the division is accomplished by subtraction:  $Log(Image) - Log(Background)$ . This type of correction assumes the scene is composed of an homogeneous background and relatively small objects brighter or darker than the background. There are two major types of background subtraction techniques depending on whether the illumination model of the images can be given as additional images or not:

1. Prospective correction
2. Retrospective correction

Prospective correction uses additional images obtained at the image capture time.

Two types of additional images can be used:

- A dark image is an image of the scene background acquired with no light.
- A bright image is an image of the scene background acquired with light but without objects.

Going back to the case of optical detection of the flame, there was no way to acquire the background image directly, so it was decided to rely on other techniques to estimate it. Therefore, retrospective correction can use the same background subtraction method than the prospective correction with the estimated bright image. There are different algorithms for estimating the background image. All of them assume the scene background corresponds to the low frequencies and the objects to the high frequencies. The retrospective correction techniques consist in removing the objects from the original image to build the background image, and then apply the correction using this image.

Among these techniques certainly stands out the Retrospective Correction using Low-pass Filtering. The background is estimated by using a low-pass filtering with a very large kernel. The background is then subtracted from the input image to compensate the illumination. "In image processing, a kernel, convolution matrix, or mask is a small matrix. It is used for blurring, sharpening, embossing, edge detection, and more. This is accomplished by doing a convolution between a kernel and an image." def. by Ludwig Jamie, *Image Convolution* . The corrected image  $I_1(x,y)$  is obtained from the input image  $I(x,y)$  by:

$$I_1(x,y) = I(x,y) - LPF(I(x,y)) + mean(LPF(I(x,y))) \quad (3.1)$$

where  $LPF(f(x,y))$  is the low-pass filtering of image  $I(x,y)$ , and  $mean(LPF(I(x,y)))$  is the mean value of the low pass image.

The low-pass filter  $LPF(I(x,y))$  can be applied in different ways to an image. In this case it was decided to apply it using a Gaussian filter. It is characterized by a standard deviation  $\sigma$ , expressed in terms of pixel dimensions, and calculated as:

$$G(x,y,\sigma) = \frac{1}{2\pi\sigma^2} \exp^{-\left(\frac{x^2+y^2}{2\sigma^2}\right)} \quad (3.2)$$

where  $x$  and  $y$  are the distance in pixels from the center of the kernel. The size of the kernel is 3 times the standard deviation on either side of the central pixel. The example taken from the [29] in Figure 3.2 shows the result of applying smoothing with Gaussian kernels with a standard deviation of 1.0 pixel and 3.0 pixels to the same original image.

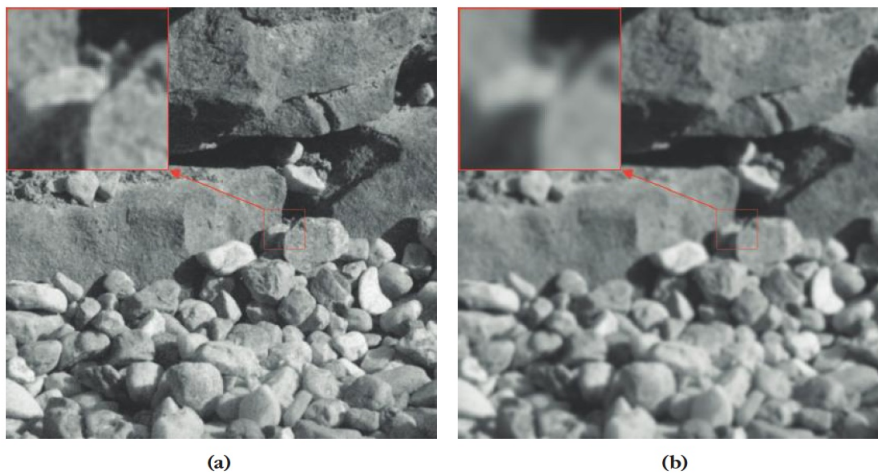


**Figure 3.2:** Figure 3.2a ( $\sigma = 1$ ) is compared to Figure 3.2b in which the standard deviation has a higher value ( $\sigma = 3$ )

For the case analyzed, the correct standard deviation value was chosen by sensitive analysis. The choice fell on a sigma of 10, because with this sigma value in the background image the chessboard of the calibration is no longer recognizable, but only a background of colors that reflects the trend of the color intensity from left to right. Smaller sigma results in an image in which the calibration paper chessboard is too sharp. Larger sigma leads to loss of information even on the intensity trend, resulting in a monochromatic image.

In matlab environment, to apply a Gaussian filter there is a function called *imgaussfilt* that filters an input image with a Gaussian smoothing kernel with standard deviation specified by sigma. Below there is an example of a typical background image in the case of sigma of 10 (Fig.3.3). Applying this function requires an input image. The image available is an indexed integer image. Txt files are read as matrices in two dimensions in which each element represents a color gradation value for each pixel. Based on the theory of retrospective correction (3.1), the next step will be to subtract the background from the input image (Fig.3.4). In matlab it is possible to simply use the *imsubtract* function with input the starting image and the image to be subtracted. Finally, the last step consists in adding to the intermediate image the average of the background image (3.1), which is a constant value. In the Figure 3.4 and 3.3 a visual comparison was made between the original image on the left in 3.3 and the corrected image on the right in 3.4. All the pictures have been inverted with respect to the vertical symmetry axis. (Matlab code in Appendix A.1).

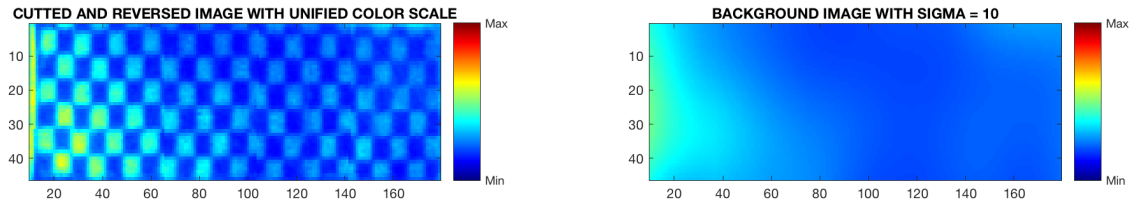


**Figure 3.3:** On the left there is the original calibration image, in case of  $Pc = 10$  bar e  $OF = 4.4$ , while on the right there is the corresponding background with  $\sigma = 10$

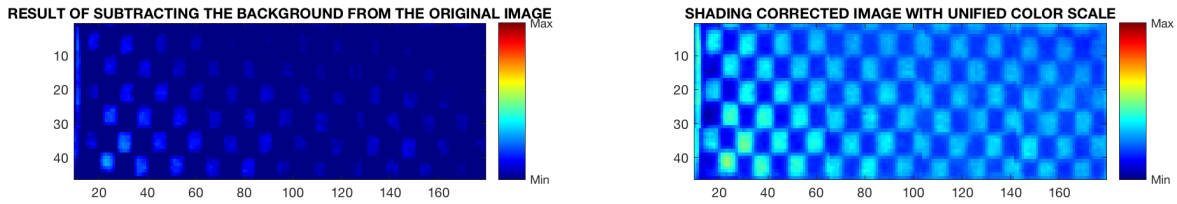


**Figure 3.4:** On the left there is the corresponding image resulting from the subtraction with background with  $\sigma = 10$ , while on the right there is the corresponding image with shading correction

The accomplishment of shading correction can be demonstrated by using a graph in which the x axis represents the horizontal dimension of the window in pixel terms, and the y axis the intensity of pixels along the window's length. So, the curve in each chart is unique, because it represents the average value for each column of the picture, and it stand for the brightness trend in the space. The Figure 3.5 shows a comparison between the graph of the original image and the graph of the corrected image in the same conditions of the previous example ( $Pc = 10$  bar and  $OF = 4.4$ ). The curve in the corrected image has a slight increase in the left part of the photo, where the brightness appears higher than the right side. The curve appears flat, although with some oscillations, compared to the original case in which the curve grow at the brightest part. By making a quick comparison, the peak values reached in the left side of the photo are lower than the original case. While the peak values of the right side of the photo, practically where the shadow is present, are higher than the original picture. This says that the corrected image has values that are less distant from the average value, and tendentially the image is more intense where previously it was less, and vice versa. The image finally appears more homogeneous. In summary, the shading correction process is developed, for each case analyzed, always starting from the calibration image. Through the visual sensitive analysis of the calibration image, a suitable sigma to correctly estimate a background image was chosen: 10. The background image will be very important for a retrospective correction because, if properly created, it leads to a balancing of the brightness of the image; in the example above, it is possible to see the real advantages that shading correction brings to the calibration image. To continue, it

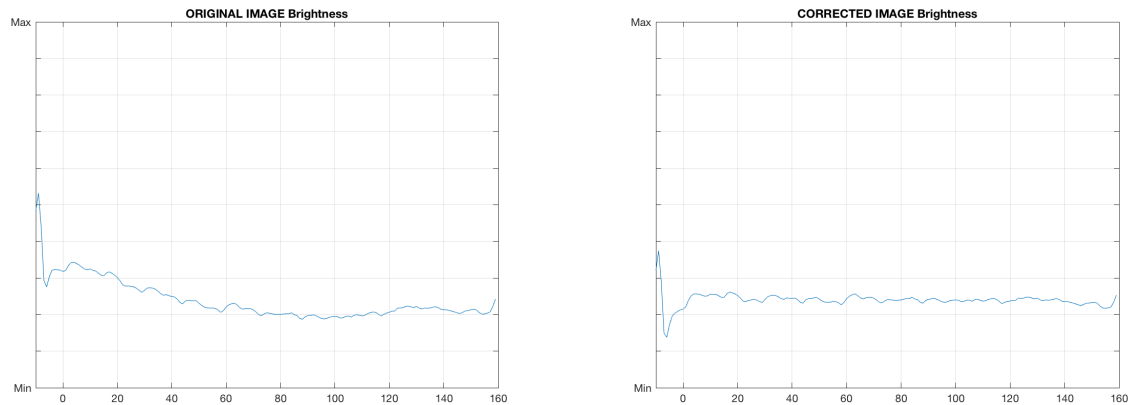


**Figure 3.5:** On the left is shown the brightness of original image along  $x$ ; on the right there is the brightness graph of corrected image

will be necessary to correct the captured images of the flame, which are the true objective of this thesis. In this context the work done so far has not only been an effective proof of the success of the correction, but will have produced a background image necessary for flame correction. Naturally, the background produced from the calibration image will be useful for the flame captured under the same lighting conditions as that calibration. So for each test there will be a captured image of the flame, a corresponding calibration image and a background image created from the calibration. Instead it is necessary to use a background, which as the word itself says, represents the inhomogeneous conditions of the background brightness. These conditions are visible only when the flame is not yet present, and therefore in the calibration image. The flame, which will be the main subject of the analysis, will itself be influenced by this inhomogeneous background luminosity. Then we will proceed with the elimination, from the photo of the flame, of this layer of non-homogeneous brightness. The same steps as before will be performed, only that the background of the corresponding calibration image will be subtracted from the original image, saved on disk (Fig. 3.6). And of course for the last step, the average of the same background image will be added. Finally, the correct image of the flame will be obtained (Figure 3.6).

Through the calibration image, a certain light inhomogeneity has been noticed. More light is present in the left part of the photo, while on the right there is an area characterized by low brightness. So the flame displayed in the original picture is influenced by this inhomogeneity. Once the correction is applied, the image looks like it should actually appear. On the left, without that extra brightness, you can no longer observe the anchor points of the flame. On the other hand, on the right, with more light, the flame appears

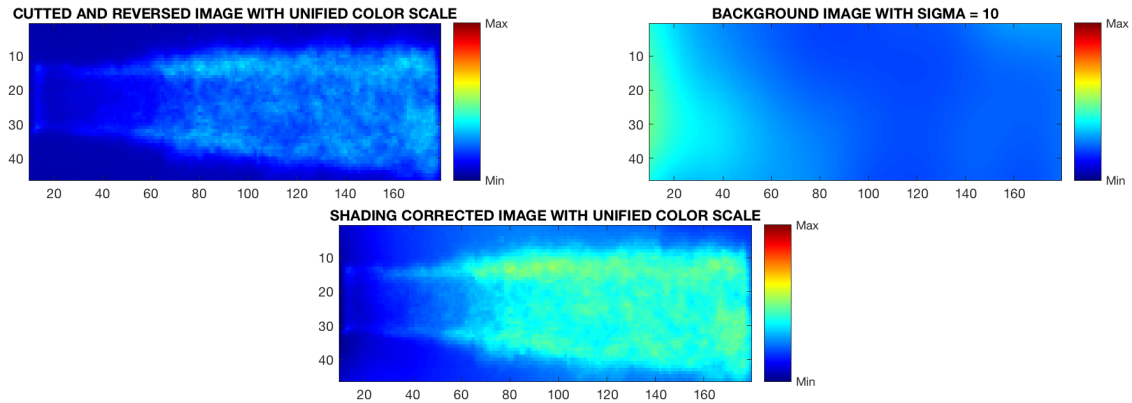


**Figure 3.6:** On the left there is the original flame image, in case of  $P_c = 10$  bar e  $OF = 4.4$ , on the right there is the corresponding background with  $\sigma = 10$ , while below is shown the corresponding image with shading correction

slightly brighter. So overall it can be said that the flame detection was influenced by the light inhomogeneity.

To have another comparison parameter, it was applied the correction to the results from another test. The test in question is the one carried out at chamber pressure of 20 bar and  $OF = 6.0$ ; this test is the most extreme (closest to stoichiometric condition) of the entire experimental campaign, and therefore the captured flame is the brightest. The process will be identical to the one already explained. The Figure 3.7 shows the detection of the background with the usual  $\sigma = 10$  and the validity is always confirmed by the graphs in the Figure 3.8, which confirm the brightness regulation along the axis. Subsequently, in the Figure 3.9, the flame detected under the same conditions is corrected, using the newly constructed background. Also in this case the brightness, originally greater in the left part, had influenced the detection of the flame. After correction, the left part of the flame is less bright, as it should have been originally.

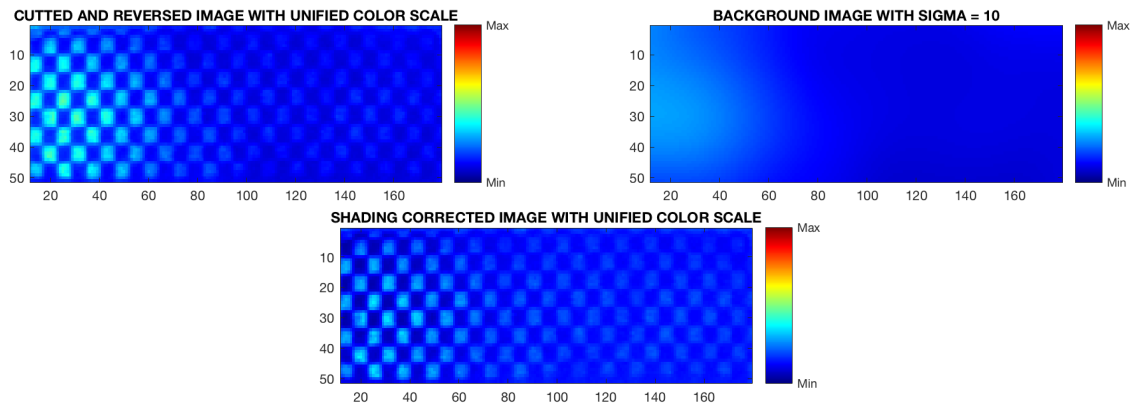


**Figure 3.7:** The image at the top left shows the original calibration image; the image at the top right shows the background constructed starting from a Gaussian filter with  $\sigma = 10$ ; the photo below shows the corrected calibration image.

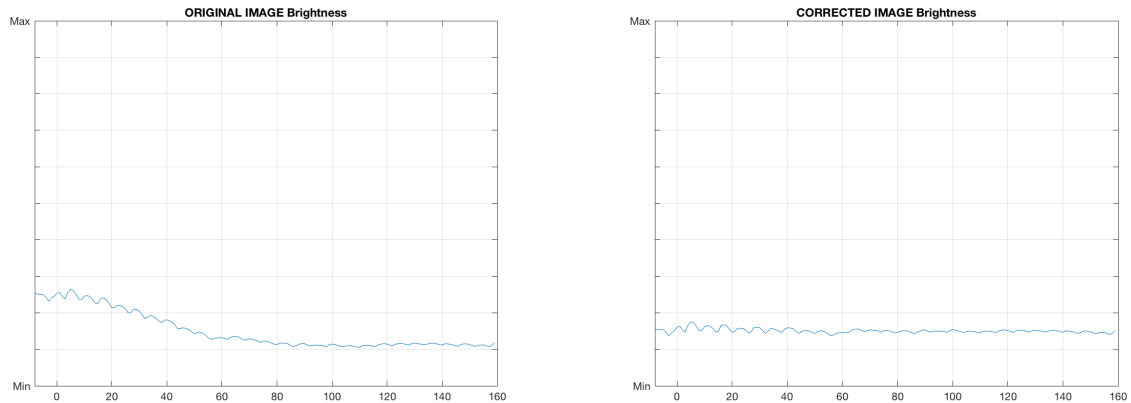


**Figure 3.8:** On the left is shown the brightness of original image along x; on the right there is the brightness graph of corresponding corrected image

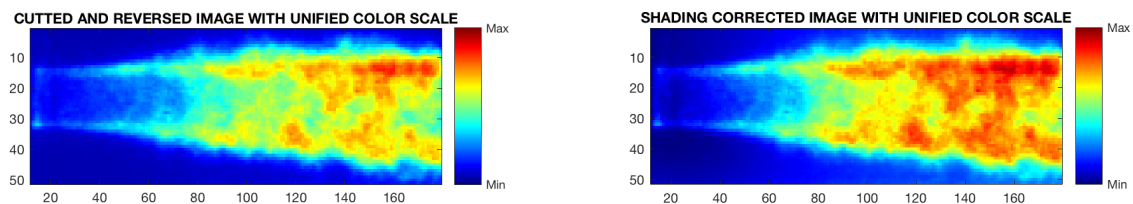


**Figure 3.9:** On the left there is the original flame image, in case of  $P_c = 20$  bar e  $OF = 6.0$ , while on the right there is the corresponding image with shading correction

As has been anticipated in the introductory part of this paragraph, the procedure for the digital camera’s pictures is the same. The piece of code concerning the digital camera is attached in the Appendix A.2. Minimum differences are used in the operations, having in this case an input image with punctual values in a range from 0 to 255 (RGB colors),

it is necessary to convert the image into a double image with precise values from 0 to 1. The matlab function *imdouble* is useful for this purpose. The obtained background image is practically the same as before (Fig. 3.10). There are two small differences in the subsequent applied operations: since the new values to be managed will be decimal values, where first a subtraction was used to eliminate the background from the original photo, in this case a division will be used (Fig. 3.11). So as where previously the average value of the background was added to obtain the correct image, in this case the average value will be multiplied to obtain the correct image (Fig. 3.11). In the example shown below, for the case  $P_c = 20$  bar and  $OF = 4.4$ , the results will be completely identical and you will be able to obtain a lightening of the darker areas and at the same time a homogenization of the brightness of the photo of the flame.

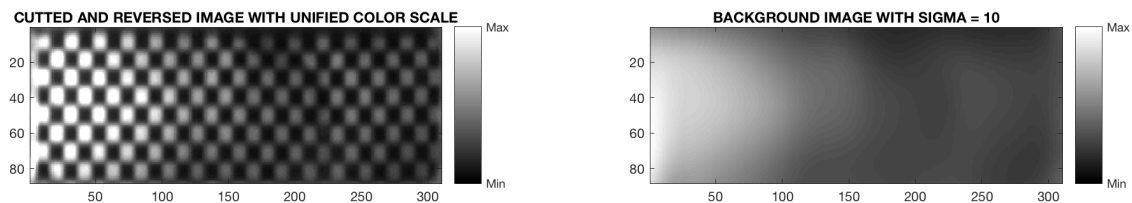


**Figure 3.10:** On the left there is the original calibration image, in case of  $P_c = 20$  bar e  $OF = 4.4$ , while on the right there is the corresponding background with  $\sigma = 10$

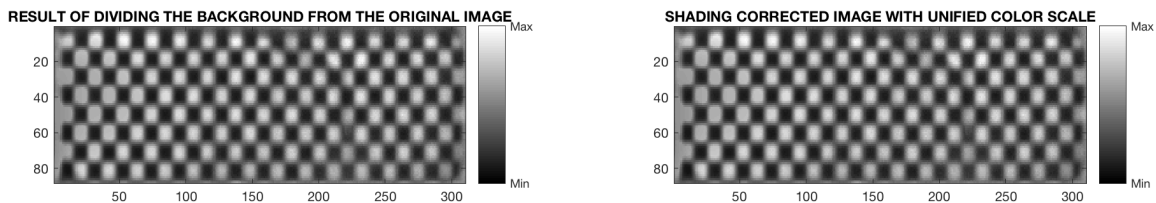


**Figure 3.11:** On the left there is the corresponding image resulting from the division with background with  $\sigma = 10$  (3.10), while on the right there is the corresponding image with shading correction

Naturally, as in the previous case, the diagrams of the brightness are useful to understand the actual success of the correction. The Figure 3.12 shows the trend along the x axis of the brightness. The flattening of the curve indicates the good result obtained thanks to the shading correction.

To conclude the process was then applied to the image of the flame, thanks to the use of the background previously created, returning a correct and brighter image where previously there was a shadow (Fig. 3.13).

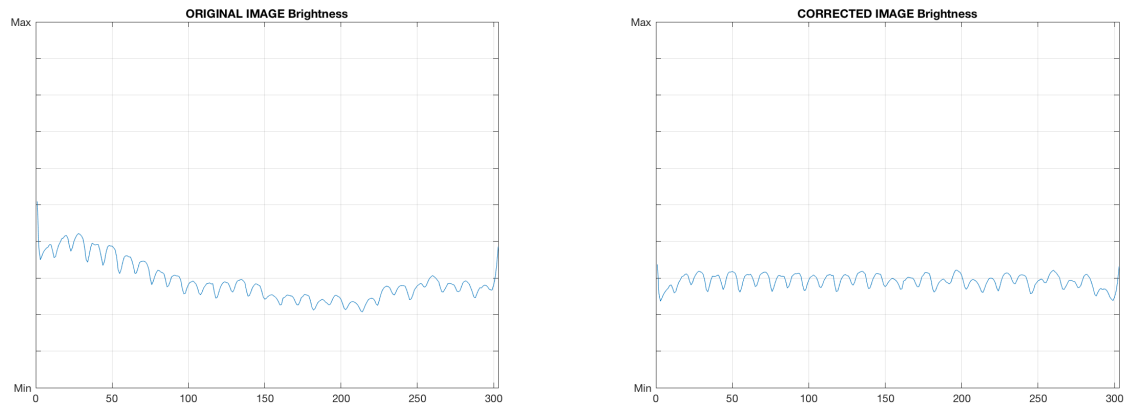


**Figure 3.12:** On the left is shown the brightness of original image along  $x$ ; on the right there is the brightness graph of corrected image

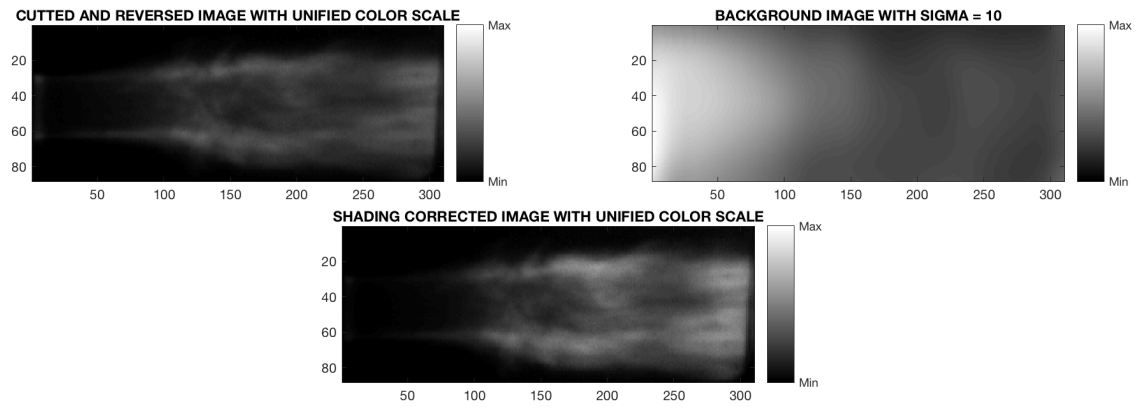


**Figure 3.13:** On the left there is the original flame image, in case of  $P_c = 20$  bar e  $OF = 4.4$ , on the right there is the corresponding background with  $\sigma = 10$ , while below is shown the corresponding image with shading correction

## Chapter 4

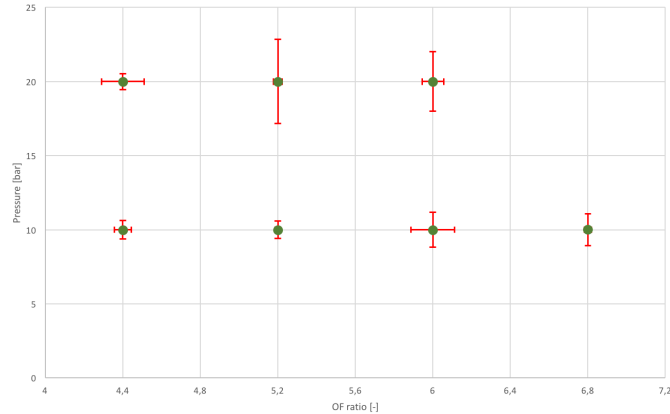
# Operative Conditions and Test Results

All test loadpoints were performed twice, one for each camera calibrated. Sonic orifices in oxidizer and fuel feed lines and corresponding upstream pressure values set mass flow rates inside the combustion chamber. A burning time of 2 seconds, limited because of the capacitive nature of the combustors, is set for all hot firing tests, as well as the same test sequence is used, except for film coolant injection. An ignition duration of 300 ms at minimum igniter power is set to achieve the start up condition and to minimize the igniter's influence on the evaluation procedure. Due to the transient behavior of the hardware, for the evaluation of the test data three time intervals are defined: a time  $t_0$  for initial conditions, a time  $t_1$ , named evaluation time, characteristic for the hot run and a time  $t_2$  for shutdown condition. The time  $t_1$  is conventionally taken at  $2/3$  of the hot run. To minimize the influence of the transient start up, the performance parameters as well as temperature and pressure distribution along the combustion chamber axis are calculated as mean values over a  $-0.25 t_e + 0.25 t_e$  time interval with  $t_e =$  evaluation time. Film cooling has been set when the rectangular combustion chamber was tested in order to prevent crack enucleation and propagation inside the optical access quartz glass window. As already announced in Chapter 2, run-in tests were performed at nominal combustion chamber pressure ( $P_c$ ) of 10 and 20 bar, with mixture ratio (OF) of 4.4, 5.2, 6.0 and 6.8 (only for chamber pressure of 10 bar). A resume of the test matrix is outlined in Fig. ?? and Table 4.1. A 20% film coolant mass flow rate with respect to the fuel mass flow rate is set for all run-in tests conditions. In addition, no film cooling routines are performed for mixture ratios 4.4 and 6.0, at 20 bar pressure level.

	OF = 4.4	OF = 5.2	OF = 6.0	OF = 6.8	
<i>10 bar</i>	■	■	■	■	■ 20% film
<i>20 bar</i>	■□	■	■□		□ 0% film

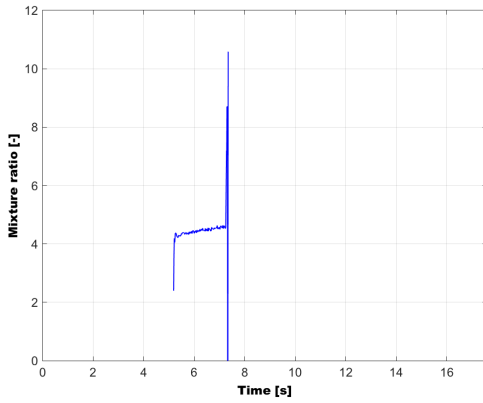
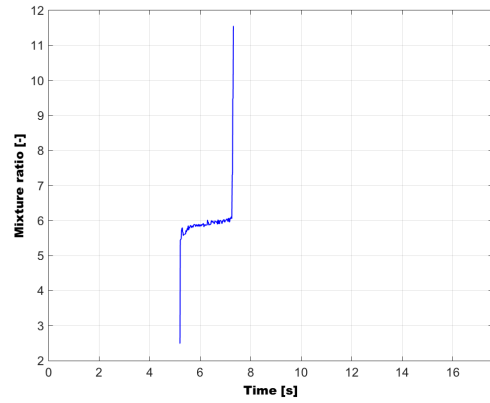
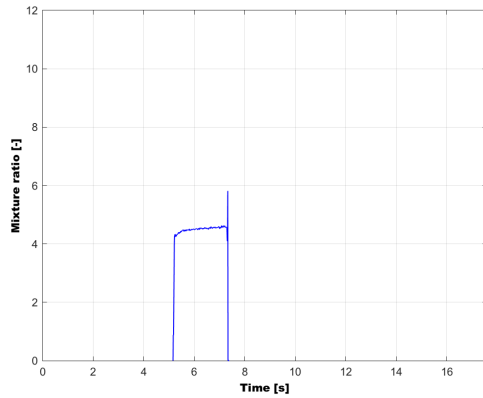
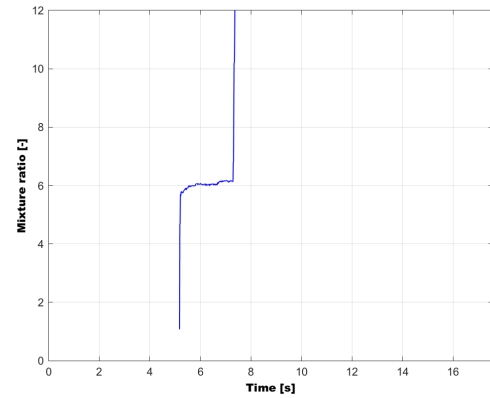
**Table 4.1:** Test nominal points

Naturally, the load points shown in the Figure 2.5 are only nominal points. In practice, the non-standard environmental conditions, the almost never perfect operation of the equipment and the acquisition of data characterized by a certain level of error, implies that the actual values of the load points are approached only approximatively to the nominal ones. In fact, as shown by the error bars in the figure 4.1, during each test, both the pressure and the mixture ratio vary within two limit values.



**Figure 4.1:** Nominal load points with error bar

This may be due to many factors: external environmental conditions such as to vary the pressure in the oxidizer and fuel tanks (these vary in density depending on the outside temperature and therefore the pressure varies inside the tank with respect to the known one). There could also be other causes, such as the presence of small leakages not detected in the combustion chamber or the low sensitivity of the pressure regulator used to set the injection pressure, thus leading to pressures and therefore the actual mass flow rates different from those set. Pressure are set manually and that is not very precise and for this reason are used not experimental data and not nominal ones to evaluate results. The fact that the tests are not instantaneous, but have a certain temporal duration, mean that during the detection time the value in question is not fixed but varies over time. An example of this is given in the Figure 4.2, where the trends over time of mixture ratios 4.4 and 6.0 are displayed for both pressures in the combustion chamber.

(a)  $P_c = 10$  bar,  $OF = 4.4$ (b)  $P_c = 10$  bar,  $OF = 6.0$ (c)  $P_c = 20$  bar,  $OF = 4.4$ (d)  $P_c = 20$  bar,  $OF = 6.0$ **Figure 4.2:** Some examples of mixture ratio trends in time

In the graphs, a trend is observed that increases over time until the nominal value is reached after a certain time transient. At initial instants the mass flow rate of oxygen is less than it should be, or vice versa for hydrogen. During the burning time the quantities become the nominal ones in a transient. Furthermore, the correct values pressure of oxygen, hydrogen and nitrogen at the injection were set by means of pressure regulator. The values were based on an experimental database, calculated in such a way to have the chosen mixture ratio. The environmental conditions, and an external temperature close to zero, have changed these standard pressure values. Therefore, to obtain the correct mixture ratio value, more tests have to be carried out by varying the pressures through the pressure regulator.

Since mixing efficiency of a shear coaxial injector is mainly due to the shear forces between oxidizer and fuel flows, non-dimensional parameters are employed and preliminary evaluated: Velocity Ratio (VR) and Momentum Flux Ratio (J), defined as in Eq. 4.1 and

Eq. 4.2, are depicted in Fig. 4.3 for different mixture ratios at 10 and 20 bar test cases. Both the parameters are based on the propellants inlet parameters.

$$VR = \frac{u_{GH2}}{u_{GOX}} \quad (4.1)$$

$$J = \frac{(\rho u^2)_{GH2}}{(\rho u^2)_{GOX}} \quad (4.2)$$

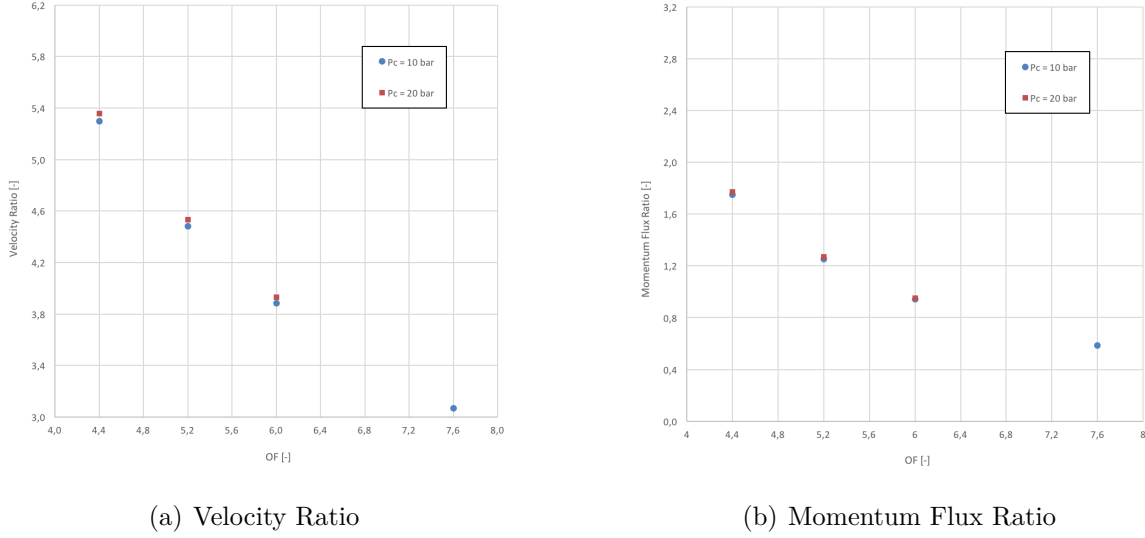


**Figure 4.3:** Velocity Ratio and Momentum Flux Ratio at different load points

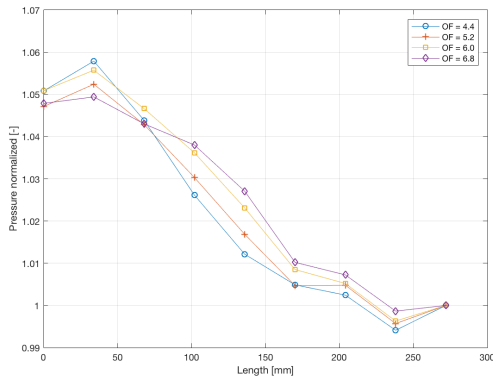
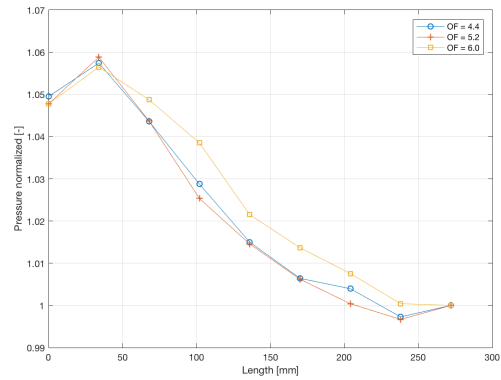
Theoretical calculations of the VR and J were carried out, in order to have further confirmation of the values obtained through Matlab code. In general, theoretical and experimental values coincide. The results are presented in the Appendix B.

Therefore, with the same  $\dot{m}_{GH2}$ , increasing  $\dot{m}_{GOX}$ , and therefore increasing ROF, the oxygen flow speed increases compared to the hydrogen one and then velocity ratio VR and the momentum flux ratio J decrease.

## 4.1 Pressure Distribution along Chamber Axis

In order to better understanding the combustion chamber process, it is necessary to normalize the chamber pressure. Three different normalizations are chosen with respect to the mean pressure, the pressure measured by the first transducer and the pressure measured by the last transducers. The first normalization is obtained dividing every value of pressure, given by each sensor, to the mean value of pressure (the pressure is measured using nine pressure sensors). In this way, it is possible to have a trend of the chamber pressure, as a function of the deviation of the pressure from the mean value. For this reason, this normalization represents the best solution. Dividing each pressure value by the value measured by the first pressure transducer (PC0), the second normalization is given. This normalization is useful to highlight the end of pressure trend, in order to analyse the end of the combustion process. The third normalization is based on the ratio between each pressure value and the pressure measured by the last transducer (PC8). In this way, it is possible to investigate the re-circulation zone.

Normalized pressure (with respect to  $P_{mean}$ ) distribution along the combustion chamber axis for nominal combustion chamber pressure of 10 bar (on the left) and 20 bar (on the right) is depicted in Fig. 4.4, with a mixture ratio variable from 4.4 to 6.0 (6.8 in case of pressure  $P_c = 10$ ).

(a) Pressure Chamber  $P_c = 10$  bar(b) Pressure Chamber  $P_c = 20$  bar

**Figure 4.4:** Normalized pressure (respect to  $p_{me}$ ) distribution along combustion chamber axis

Starting the test, the propellant is injected into the combustion chamber through the injector. Due to the abrupt variation of the cross section, the flow decelerates and the pressure increases, so the flow change its direction, creating a re-circulation zone. The re-circulation zone acts to improve the mixing of the propellant and then the combustion

efficiency. This phenomenon has been exalted by the presence of the corners in rectangular combustion chamber, enhancing flow recirculation, and so more intense initial mixing of the shear layer. Moreover, the presence of a round flame in a rectangular combustion chamber could influence combustion process in the near-injector zone, where the flame is not yet adapted to the square shape. Then, the combustion process starts and lasts two seconds.

A relatively strong increase in wall pressure in the near-injection zone is visible for all run-in tests, sign of the presence of a recirculation zone. This pressure leap is equal to the difference between the maximum pressure value measured and the pressure value measured by the first transducer ( $P_{c0}$ ). The stagnation point, shown by the pressure peak, corresponds to the axial position of the re-circulation zone. Investigating the normalized pressure profiles, the mixture ratio influences the re-circulation zone. In fact, lower mixture ratios mean higher hydrogen velocity, so higher velocity ratio and momentum flux, and so more intense initial mixing of the shear layer with an higher pressure peak. Due to combustion process and consequent expansion of the gas after the injection inside the combustion chamber, the injected gases are accelerated from the injection velocity to the hot gas velocity. A decrease in the wall pressure distribution along the combustion chamber axis is expected, according to Bernoulli's equation.

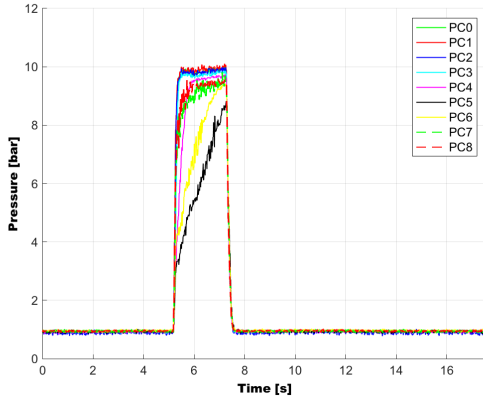
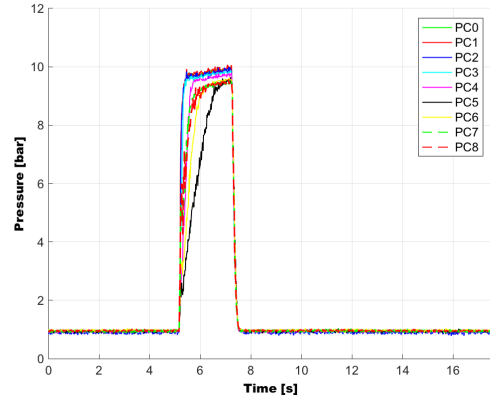
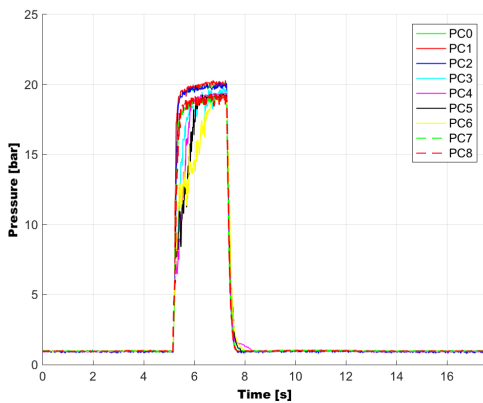
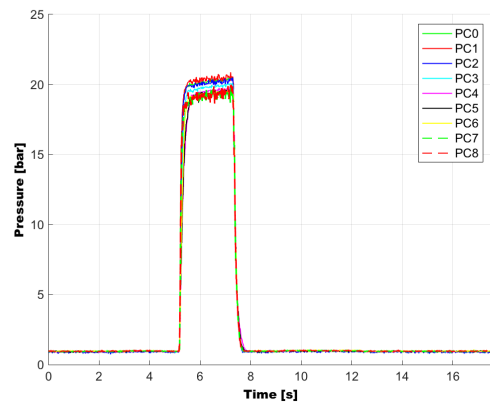
A strange behavior of the pressure detection in three specific cases is clearly visible in the graphs of the pressures detected by the nine probes over time.

The three cases are:

1. 10 bar with mixture ratio 6.0
2. 10 bar with mixture ratio 6.8
3. 20 bar with mixture ratio 5.2

Below are shown (Fig. 4.5) the cases in question (a,b,c) compared with a case in which this problem didn't happen (d). It is difficult to explain these trends due to the fact that they showed up randomly. It is certainly possible to exclude the bad functioning of the trasducers because for other tests, the detection has been correctly carried out along the whole axis of the combustion chamber. In no way is it possible to link what happened to the pressure or the mixture ratio, since this happens for different values of pressure and mixture ratio. A possible explanation could be GO<sub>2</sub> / GH<sub>2</sub> mixing problem due to a bad ignition operation. Igniter parameters were not set correctly, so an harsh ignition might cause an influence in the flame stabilization. Furthermore, it is a problem that has been observed only in cases of combustion with GO<sub>2</sub> / GH<sub>2</sub> (in this experimental campaign

and in others that have been performed in the past). For the campaign with GO<sub>2</sub> / GCH<sub>4</sub> this behavior did not occur (refer to the Pasquale Difficile thesis [4]).

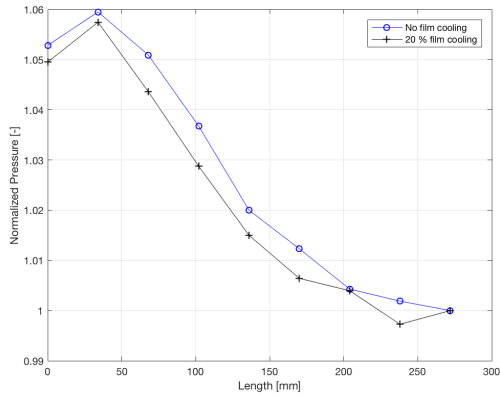
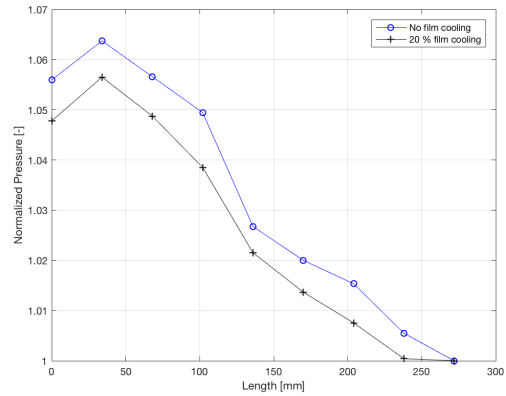
(a)  $P_c = 10$  bar,  $OF = 6.0$ (b)  $P_c = 10$  bar,  $OF = 6.8$ (c)  $P_c = 20$  bar,  $OF = 5.2$ (d)  $P_c = 20$  bar,  $OF = 4.4$ 

**Figure 4.5:** Trend in pressures, during the combustion time, detected by the nine probes along the axis of the combustion chamber

A flattening of the wall pressure, which is presumed for all load points at the last pressure transducer, is representative of the accomplishment of the combustion process along the hardware axial position. In fact, it is possible to observe a variation of the pressure gradient along chamber axis. A tendency of the pressure flattening is observed for all test cases. In particular, increasing the pressure from 10 to 20 bar, the 'plateau' of the pressure is more visible. Increasing the mixture ratio the end of combustion is moving further downstream and a decrease in the pressure gradient  $\frac{dp}{dz}$  is visible.

### 4.1.1 Film Cooling Analysis

In this paragraph a comparison between film-cooling and non-film combustion will be discussed, for the cases: chamber pressure 20 bar with mixture ratio of 4.4 or 6.0. Below, in Figure 4.6, there are the two graphs with pressure trends along the chamber axis.

(a)  $P_c = 20$  bar,  $OF = 4.4$ (b)  $P_c = 20$  bar,  $OF = 6.0$ 

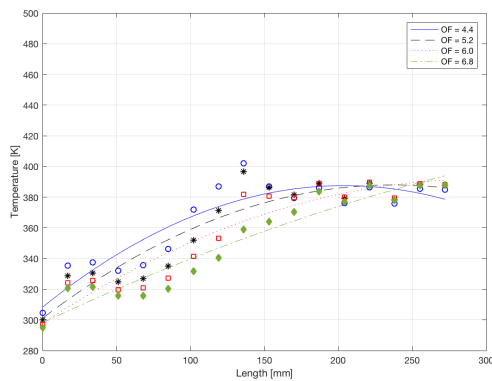
**Figure 4.6:** Pressure distribution along combustion chamber axis

The film cooling flow slightly increases the pressures in the combustion chamber because more mass flow is injected, then the  $P_{mean}$  increases and the normalized pressure trend has lower values. The same trend occurs in both cases.

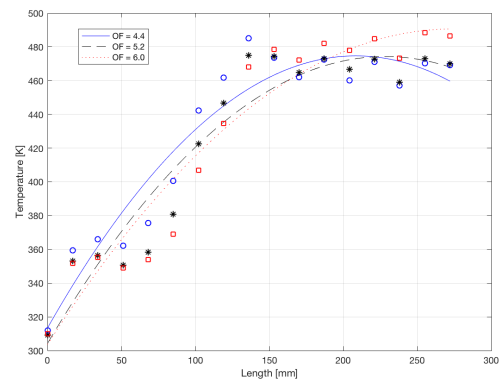
## 4.2 Temperature Distribution

### 4.2.1 Temperature Distribution along Chamber Axis

In this section, the temperature profile along the chamber axis is analyzed. Although many thermocouples are mounted on the chamber surface, type K thermocouples at 1 mm from the hot gas wall are considered for the evaluation. Temperature profile is expected to increase along the combustor axis. A flatten of the temperature trend can be associated to the accomplishment of the combustion process, as already seen for the pressure distribution along the combustion chamber axis. In order to minimize the influence of the start-up transient, the temperature signals have been calculated as a mean value over a 0.5 s time interval, taken at 2/3 of the total run time. Figure 4.7 presents temperature trends at the evaluation time, varying mixture ratio, for both cases of combustion chamber pressure.



(a) Pressure Chamber  $P_c = 10$  bar



(b) Pressure Chamber  $P_c = 20$  bar

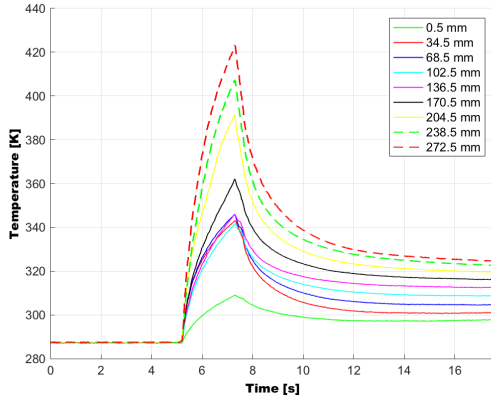
**Figure 4.7:** Temperature distribution along combustion chamber axis

For capacitive cooled hardware, a higher initial temperature leads, for the same test duration, to a higher temperature level. Therefore this aspect must be kept in mind when interpreting the results. First of all it is clear that the temperatures reached on the wall, with the same mixture ratio, are higher in the case of chamber pressure of 20 bar, with a difference between the peaks of the curves of about 100 degrees. It is clear that more pressure is present in the combustion chamber and the greater the release of heat and the temperatures reached. Analyzing temperature trends at the same pressure, it is noted that as the OF increases, the maximum temperatures reached are higher, but the consequent flattening of the curve is found in a more downstream position. In the Figure 4.7a it is noted that with  $OF = 6.8$  the flattening of the curve is almost not noticed, a sign that the accomplishment of the combustion process takes place practically at the end of the

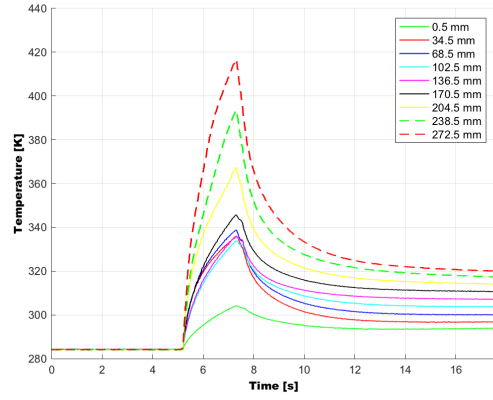
combustion chamber. Instead for  $OF = 4.4$  the accomplishment of the combustion process occurs at just over half the chamber. The higher temperature gradient along the chamber axis  $\frac{dT}{dz}$  corresponds with the higher pressure decay observed in the combustion chamber.

## 4.2.2 Temperature Distribution along Time

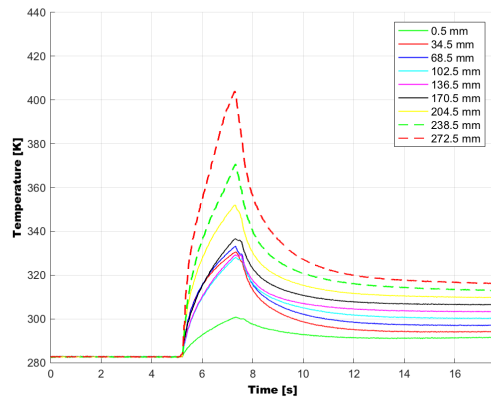
In this section, the temperature distribution during the whole test duration is analyzed. In particular, the focus is based on the temperature, measured by type K thermocouples positioned at 1 mm from the hot surface of the chamber along the chamber axis during firing.



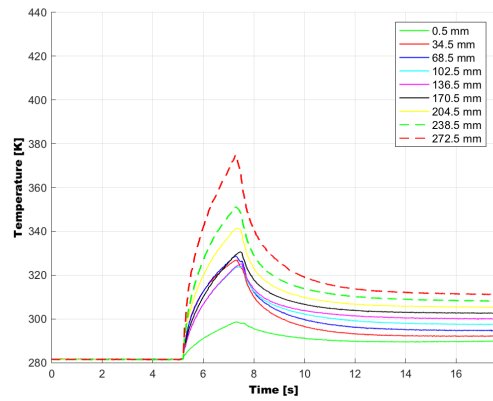
(a)  $P_c = 10$  bar,  $OF = 4.4$



(b)  $P_c = 10$  bar,  $OF = 5.2$



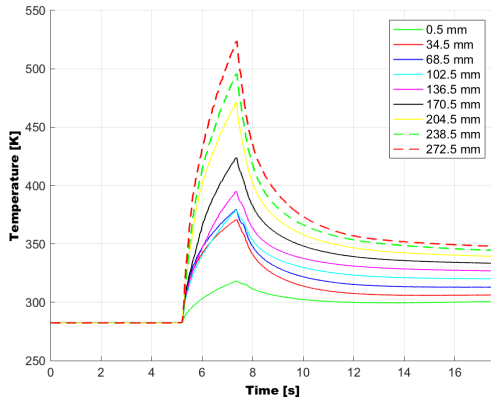
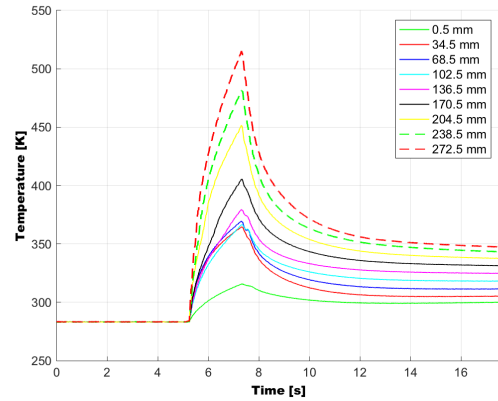
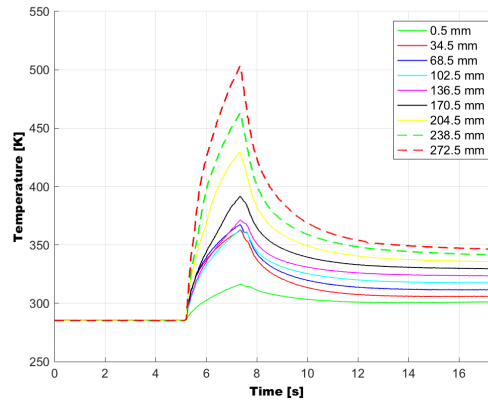
(c)  $P_c = 10$  bar,  $OF = 6.0$



(d)  $P_c = 10$  bar,  $OF = 6.8$

**Figure 4.8:** Temperature profiles for 10 bar cases, during combustion time, detected by the nine probes along the lower side of the combustion chamber longer segment

Temperature profiles for different mixture ratios are shown in the case of pressure in the combustion chamber equal to 10 bar in the Figure 4.8, and in the case of pressure equal

(a)  $P_c = 20$  bar,  $OF = 4.4$ (b)  $P_c = 20$  bar,  $OF = 5.2$ (c)  $P_c = 20$  bar,  $OF = 6.0$ 

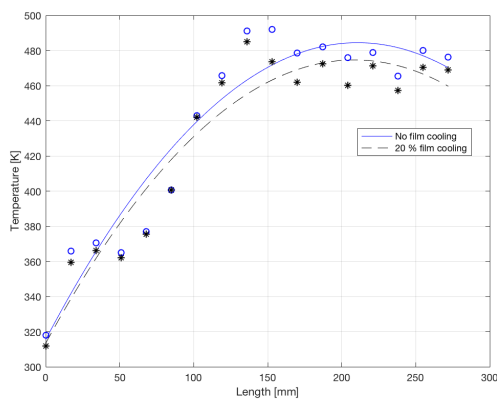
**Figure 4.9:** Temperature profiles for 20 bar cases, during combustion time, detected by the nine probes along the lower side of the combustion chamber longer segment

to 20 bar in the Figure 4.9. For all temperature traces, it is possible to identify two main temperature gradients. In the first second after ignition, the temperature profile has a steeper increase, as the thermal wave travels through the chamber wall. Then, a smoother temperature increase is observed, during the remaining running time. The increasing of temperature ends when the temperature peak is reached, which indicates the end of the test. Furthermore it can be noticed that the curves slope decreases during combustion time (2 seconds), until the peaks are reached and combustion ended. The same trend could be identified in each temperature signal in the first and second chamber segments. After the test end, indicated by a decreasing of the temperature distribution, a plateau temperature is reached. Differently from the pressure trend along time, the temperature profile is not characterized by a 'plateau', which persists during all burning time. This temperature behaviour is due to the nature of two capacitive combustion chamber segments because

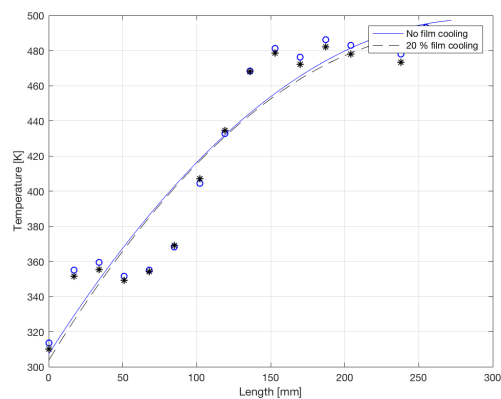
they are composed of copper free-oxygen, which is characterized by a higher thermal conductivity. In any case, note that the highest temperature is always reached by the last thermocouple. Furthermore, the maximum temperature measured by each thermocouple is always reached at the end of the burning time. Naturally the temperatures reached by the thermocouples are higher for a pressure of 20 bar in the combustion chamber. This difference between the temperature peaks decreases more and more for the previous thermocouples, until it becomes almost null for the first thermocouple. As regards the variation of mixture ratio with the same pressure, the trend is similar in both cases. In fact, as the OF increases, the temperature peaks attained by each thermocouple are always lower, up to being minimal for the case of  $OF = 6.8$ , for 10 bars, and  $OF = 6.0$  for 20 bars. This is because, as already seen in the paragraph of temperature profiles along the axis (4.2.2), as the mixture ratio increases, the combustion process accomplishment is placed in a more downstream position; therefore the heat is released more and more downstream (until to reach the combustion chamber end) and during the burning time the combustion chamber reaches lower temperatures.

### 4.2.3 Film Cooling Analysis

Comparing the results of the cases with and without film cooling (Fig. 4.10), there is a common behavior for both load points: the difference in temperature is 10 degrees maximum only in the case, ie at 20 bar with  $OF = 4.4$ . Even only about 5 degrees in the case 20 bar with  $OF = 6.0$ . This means that the impact of film cooling is not as important as one would expect.



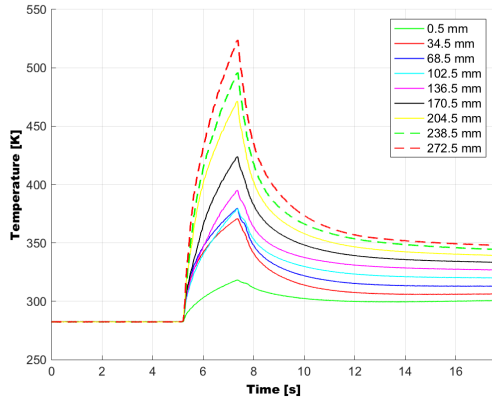
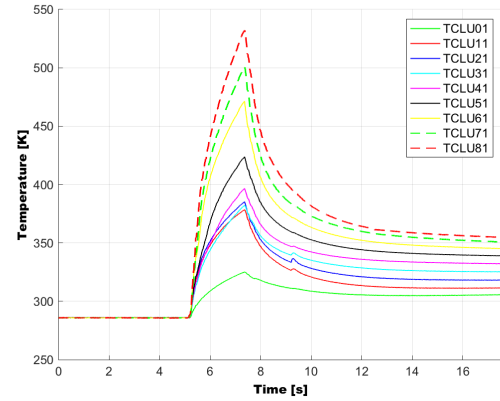
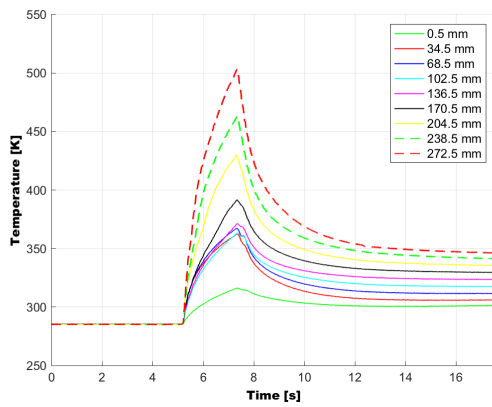
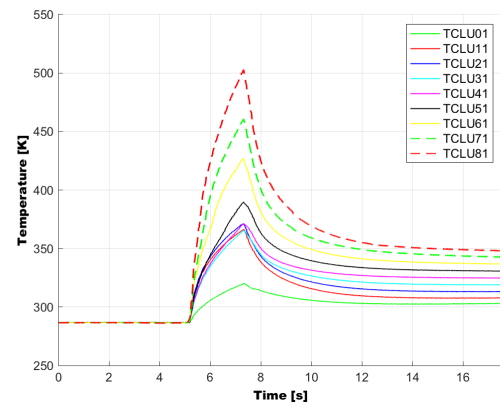
(a)  $P_c = 20$  bar,  $OF = 4.4$



(b)  $P_c = 20$  bar,  $OF = 6.0$

**Figure 4.10:** Temperature distribution along combustion chamber axis

In any case, the difference between the curves is almost imperceptible to the initial part of the chamber, where temperatures are lower. The difference starts to be noticed in the final part of the combustion chamber, that is where the temperatures are higher. The maximum temperature difference of 10 degrees is reached in the case of a mixture ratio of 4.4, since it was precisely in the case of a mixture ratio of 4.4 that higher temperatures were reached (Fig. 4.11) (Par. 4.2.2). Therefore in this case film cooling is more active.

(a)  $P_c = 20$  bar,  $OF = 4.4$ (b)  $P_c = 20$  bar,  $OF = 4.4$ , NO FILM(c)  $P_c = 20$  bar,  $OF = 6.0$ (d)  $P_c = 20$  bar,  $OF = 6.0$ , NO FILM

**Figure 4.11:** Trend in temperature, during combustion time, detected by the nine probes along the lower side of the combustion chamber longer segment

The temperature trends over time with film cooling and without, do not change almost at all (Fig. 4.11).

### 4.3 Combustion Efficiency

To describe the performance of a combustion chamber one of the parameters to look at is the combustion efficiency  $\eta_{c^*}$ . The combustion efficiency is a measure of the effectiveness of a combustion chamber to convert the internal energy contained in the fuel into heat energy [2] and may be defined as the experimental characteristic velocity,  $c_{exp}^*$ , divided by the theoretical  $c_{theo}^*$  (Eq. 4.3). The experimental characteristic velocity is defined as in Eq. 4.4.

$$\eta_{c^*} = \frac{c_{exp}^*}{c_{theo}^*} \quad (4.3)$$

$$c_{exp}^* = \frac{p_{tot} A_{th}}{\dot{m}_{tot}} \quad (4.4)$$

$$c_{theo}^* = \sqrt{\frac{RT_c}{M_m \lambda} \left( \frac{\lambda + 1}{2} \right)^{\frac{\lambda + 1}{\lambda - 1}}} \quad (4.5)$$

$p_{tot}$  is the total pressure in the throat,  $A_{th}$  is the throat area and  $\dot{m}_{tot}$  is the total propellant mass flow rate injected in the combustion chamber. A theoretical calculation based on the NASA Computer program CEA (Chemical Equilibrium with Applications), is used to evaluate the theoretical characteristic velocity. This program, developed by Bonnie J. McBride and Sanford Gordon [11], considers thermodynamic states, theoretical rocket performance, Chapman-Jouguet detonations, and shock-tube parameters for incident and reflected shocks. The properties and the enthalpy of the propellants, the mixture ratio and the combustion chamber pressure are the inputs for the calculation. To estimate the combustion efficiency, the problem is simplified. In fact the problem is solved by assuming the combustion chamber with adiabatic walls. Also the boundary layer in the throat area is not considered in the evaluation of the combustion efficiency. With this correction, the values of the combustion efficiency obtained is higher [2], due to the proportionality of the characteristic velocity with the nozzle throat area. Considering an ideal condition and theoretical rocket performance, the characteristic velocity  $c_{theo}^*$  is a function of the chamber temperature  $T_c$  and the propellant properties ( $\lambda; M_m$ ) [31]. In fact, it is possible to define the ideal characteristic velocity as in Figure 4.5.

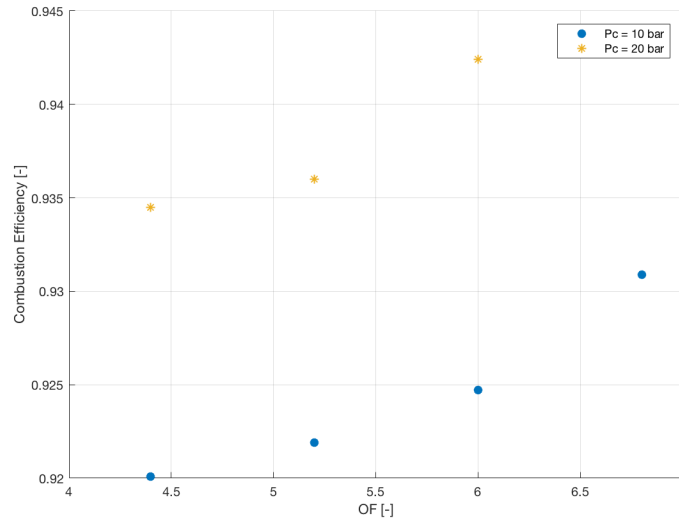


**Figure 4.12:** Combustion efficiency values for each load points

In Figure 4.12 there is a graph in which the values of calculated combustion efficiency are specified, for each of the seven load points. In particular, it is possible to use the graph to understand how the combustion efficiency varies with the variation of the mixture ratio, maintaining a constant pressure, or how the efficiency varies from 10 bar to 20 bar, with the same mixture ratio. Keeping the chamber pressure constant and increasing the mixture ratio, the combustion efficiency increase. An increase in the mixture ratio means a higher quantity of fuel, which causes a decrement in the ratio between the chamber temperature and the molar mass ( $\sqrt{\frac{T_c}{M_m}}$ ). According to the definition of the ideal characteristic velocity, represented by Equation 4.5, assuming a constant specific heat ratio, it is possible to confirm that the ideal characteristic velocity decrease and combustion efficiency increase (Eq. 4.3), with the increasing of the mixture ratio. On the other hand, by increasing the pressure at the same mixture ratio, the combustion efficiency increases.

### 4.3.1 Film Cooling Analysis

A comparison between cooled optical window and not is also given in the assessment of combustion efficiency (Fig. 4.13). The greatest efficiency is naturally achieved in cases without film cooling, as in these cases the absence of the internal film cooling layer favors lower mass flow, and therefore a higher calculated characteristic velocity (Eq. 4.4), thus higher efficiencies (Eq. 4.3). For the temperature, having the film cooling lowered the temperature more in the case of  $OF = 4.4$ , as confirmed in the graphs of the paragraph 4.2.3, the difference between efficiency in this case appears larger.

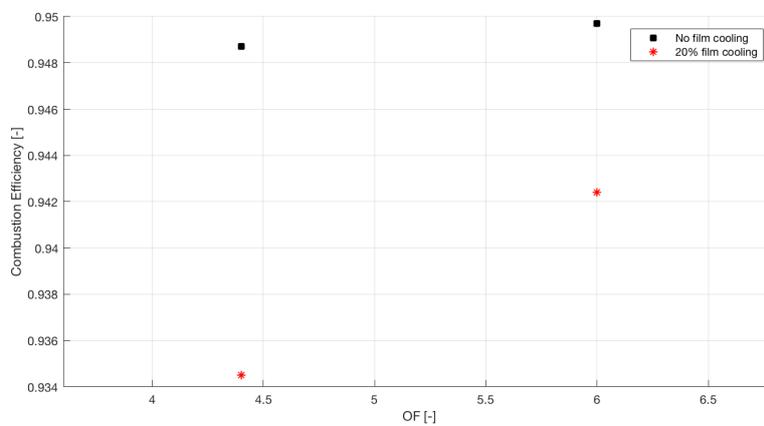


**Figure 4.13:** Comparison between combustion efficiency values

## Chapter 5

# Imaging Results and Discussion

In this chapter the results obtained through optical diagnostics will be discussed. Specifically, the post-processed photos of the Flamestar 2 camera will be analyzed to study the emissions of hydroxyl radicals  $\text{OH}^*$ , while the post-processed photos of the digital camera will be used to study the phenomenon of flame anchoring and its stabilization.

### 5.1 Flame Anchoring and Stabilization

Combustion chamber is equipped with a gaseous oxygen/gaseous hydrogen torch igniter that is fired for 300 ms. It is equipped with a supply system independent of the main injector feed system. Because the startup transient is one of, if not the most, dangerous event in the life of a rocket engine, early and safe flame anchoring and stabilization is required. A stable anchored flame is necessary to prevent blowoff or combustion instability triggering mechanisms. A digital camera was selected for the test campaign. Its light sensitivity is sufficient to capture pictures without and with different spectral filters, allowing in a low-cost way to gather good information of the combustion process with respect to flame structure. The analysis of the flame anchorage was done only for one case. The results are considered to be extensible to all other cases in question. A sequence of acquired instantaneous images are presented in Figure 5.1, for the case with a pressure chamber of 20 bar and a mixture ratio of 4.4. As can be seen in the picture sequence at 17 ms, after the igniter is activated in the middle of the combustion chamber the flame moves upstream. The ignitor is positioned in the center of the chamber, and as soon as it is activated and ignites the main combustion chamber with the flame that moves upstream. After initial oscillations, the flame anchors and gets slowly brighter with time. These initial fluctuations in the axial direction occur at a distance not longer than 20 mm from the faceplate. These picture represent the time, which ignition takes places and igniter ensure the ignition for a period of 300ms. The last picture 5.1r, however, illustrates the anchored

and stable flame, at an instant of about 1 second, then at about half the combustion time which in total is 2 seconds.

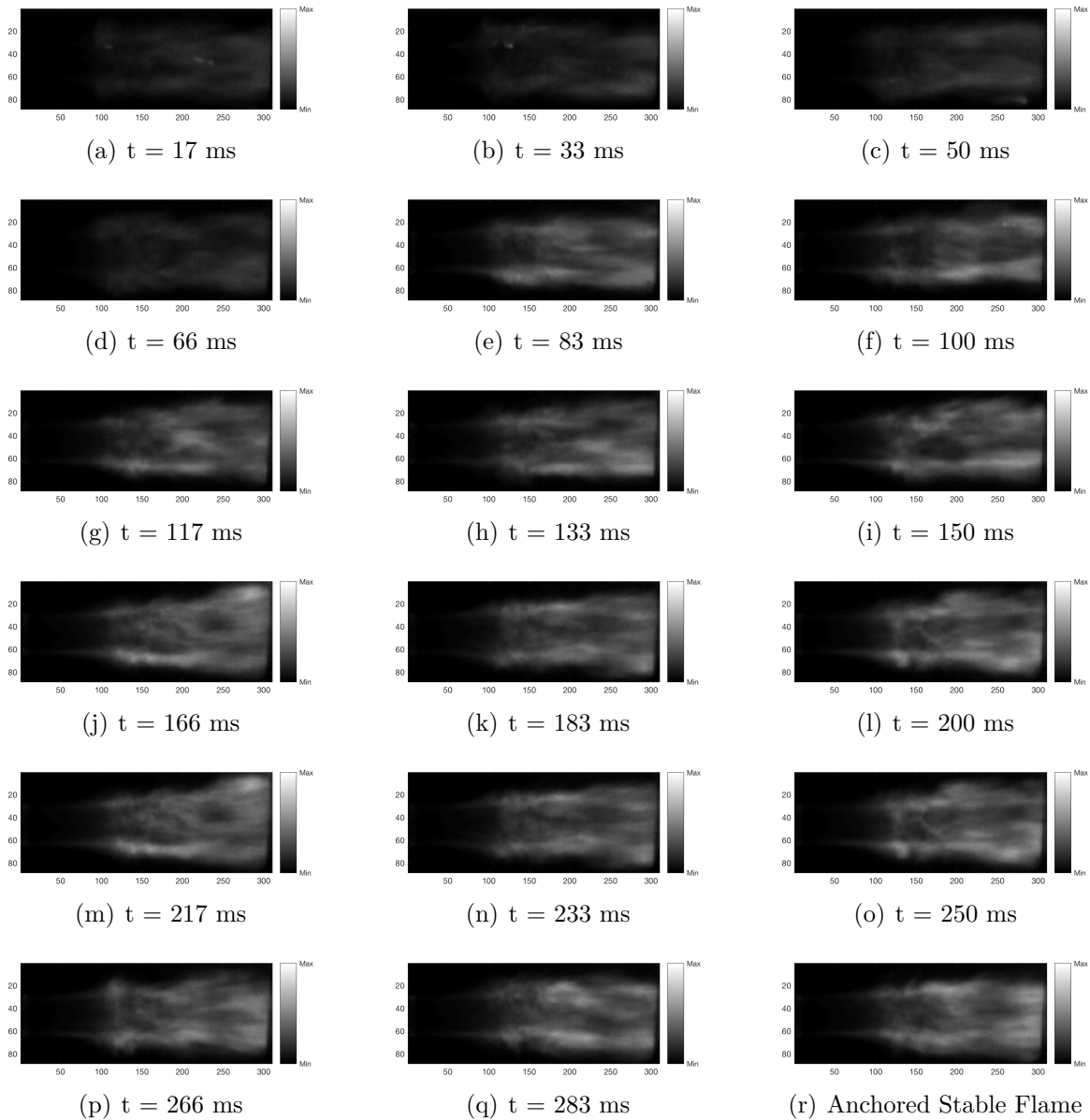


**Figure 5.1:** Start Up and Flame Anchoring for 20 bar and  $OF = 4.4$  case

Due the fact the camera has no intensifier unit, the detected light intensity at the start-up transient process is very low and therefore the flame can be properly detected only after about 100 ms of burning time. As stated by Fernanda Winter in [33]: "Previous studies have already determined that as the flow passes a step, it separates and a shear layer develops, providing a low-velocity zone for the flame to reside and propagate into the reactant flow. This recirculation zone behind the step supplies combustion radicals with enough energy to overcome the activation energy of incoming reactants, thus initiating

burning within the shear layer. The flame was attached to the wake of the GOX post-tip for all the tests performed in this investigation."

Optical diagnosis of cases without film cooling was performed with the USB camera. Therefore, in Figure 5.2 there are nine instantaneous images taken during the first 100 ms. Comparing them with the film cooling case, no anomalous flame behavior is detected. The greater luminosity of the flame that can be found in the case with film cooling is due to different lighting conditions for the two cases, since the two tests were conducted at different times during the day.

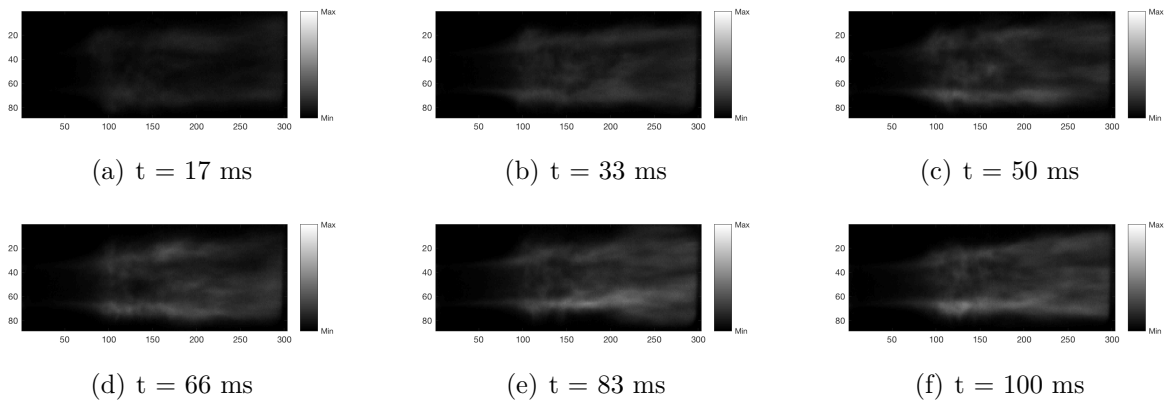


**Figure 5.2:** Start Up and Flame Anchoring comparison for 20 bar and  $OF = 4.4$  case, without Film Cooling

In the same way it was observed the shut down of the flame, with the last six instantaneous images shown in the Figure 5.3. The flame becomes gradually less luminous, and the combustion can be considered already finished when the luminous part of the flame disappears altogether, leaving only the traces of the anchor in the background (therefore roughly after the first three images). The images have been compared, as for the start up, with the corresponding test carried out without film cooling, and no difference in behavior have been detected (Figure 5.4).

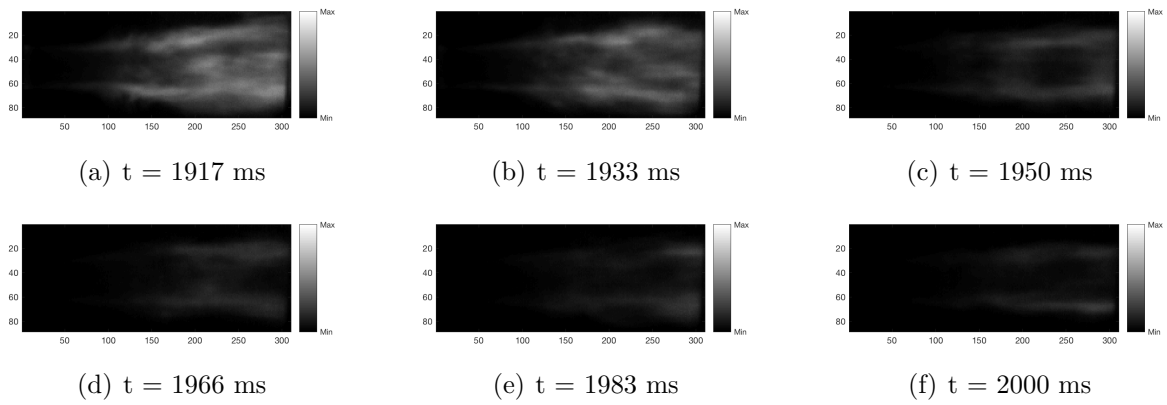


**Figure 5.3:** ShutDown for 20 bar and  $OF = 4.4$  case

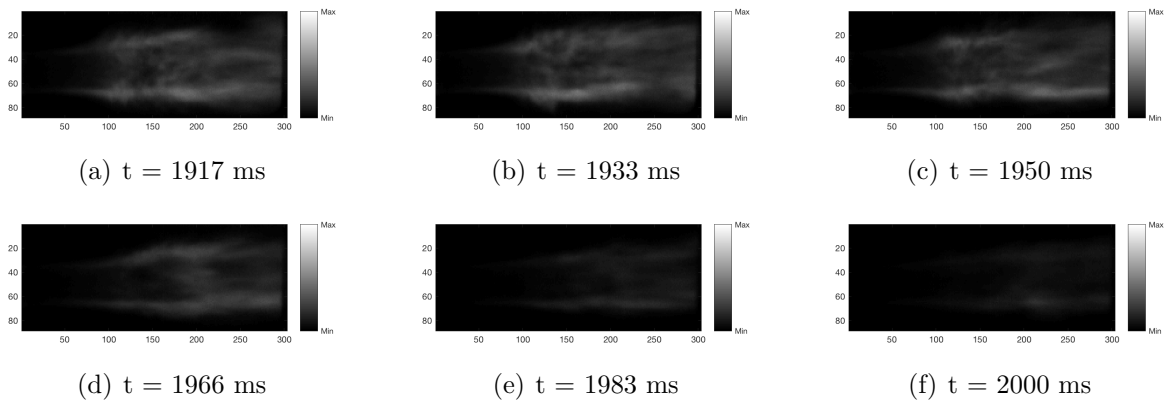


**Figure 5.4:** ShutDown comparison for 20 bar and  $OF = 4.4$  case, without Film Cooling

## 5.2 OH\* Emission

The images obtained after post processing are shown below. First the images of the flame obtained for the various mixture ratios at  $P_c = 10$  bar are shown (Fig. 5.5). And then the images for the tests with 20 bar (Fig. 5.6).

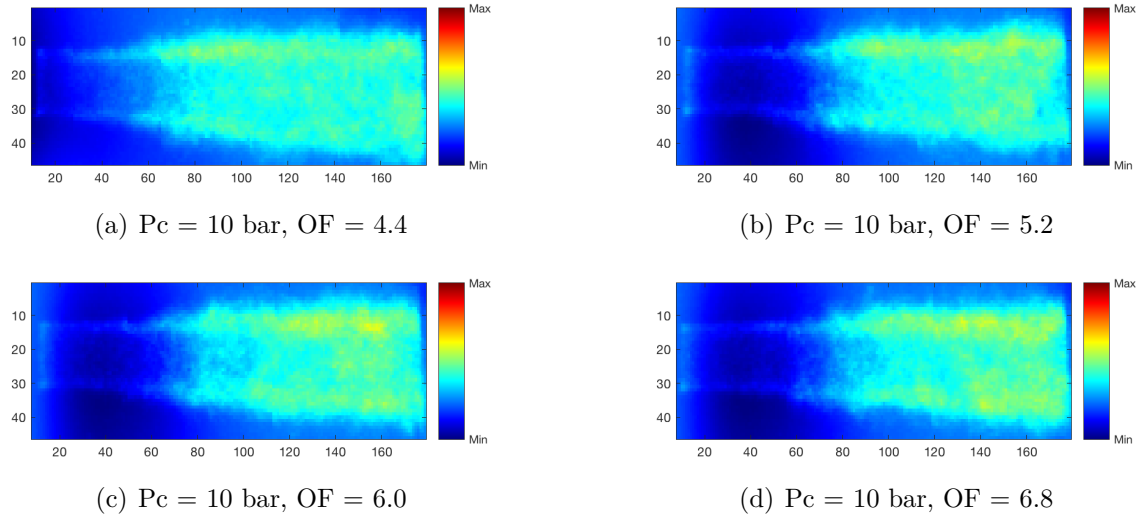


**Figure 5.5:** OH\* Emission images for each load point at a chamber pressure of 10 bar

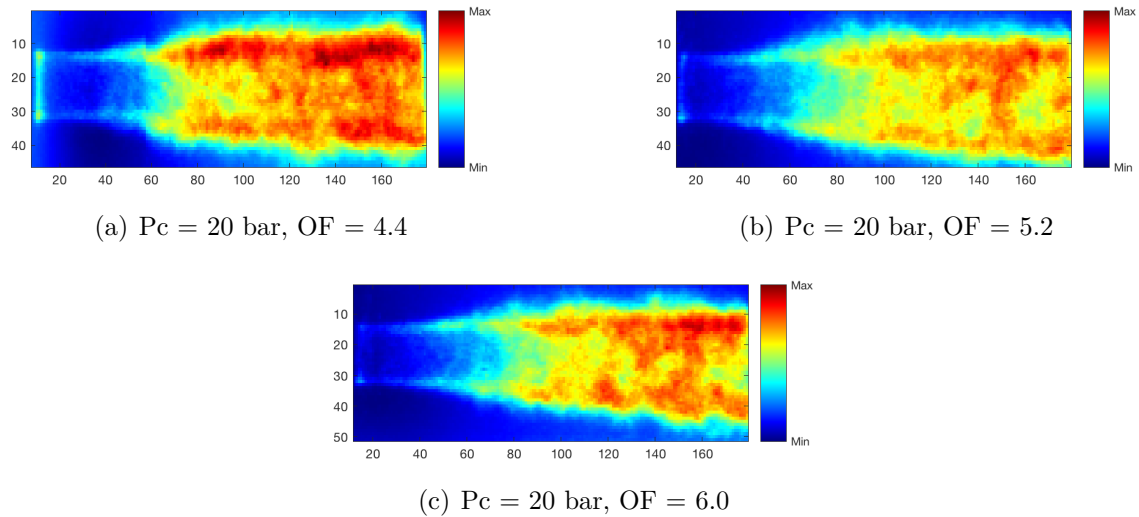
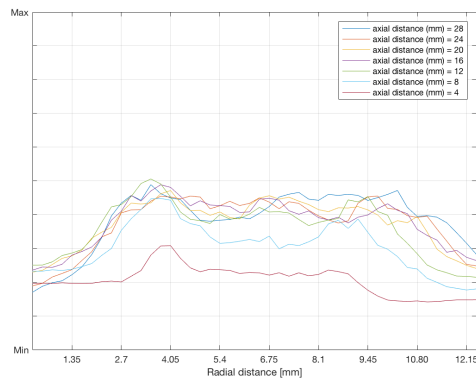


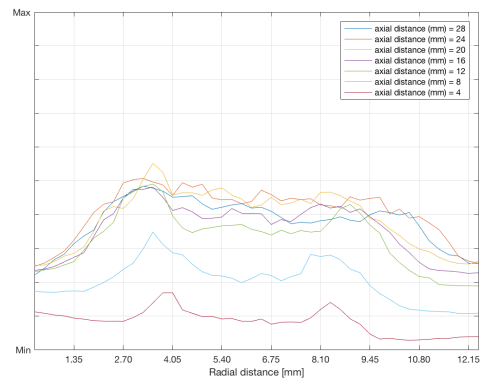
**Figure 5.6:** OH\* Emission images for each load point at a chamber pressure of 20 bar

First of all note the flame asymmetry that characterizes all the images. In fact, the upper half of the flame appears brighter in each of the seven images analyzed (Fig. 5.5 And Fig. 5.6). An explanation must be sought in the geometry of the injector which should

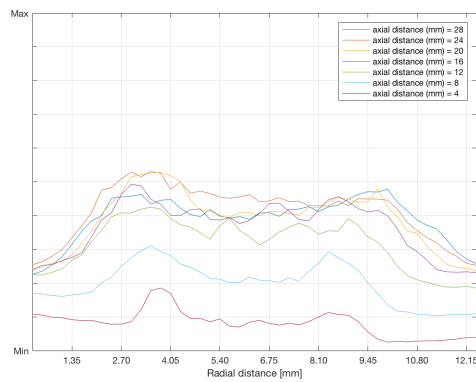
be perfectly coaxial to guarantee a symmetrical injection. Evidently the injector is not perfectly concentric and in the upper part the fuel injection is more substantial at the expense of oxygen. So an increase in the flow velocity of hydrogen increase parameters such as the velocity ratio and the momentum flux ratio. This means that there is more mixing in the upper half and therefore more OH\* radicals emitted. The confirmation of this asymmetry can be obtained from the graphs in the Figure 5.7 and 5.8 that represent the trend of emissions along the radial direction at different positions along the combustion chamber length. In correspondence of the left side, we notice the values reached on average higher than the right side; to each of the positions considered. Moreover, a significant emission increase is observed in the second part of the optical access region as the axial distance increases.



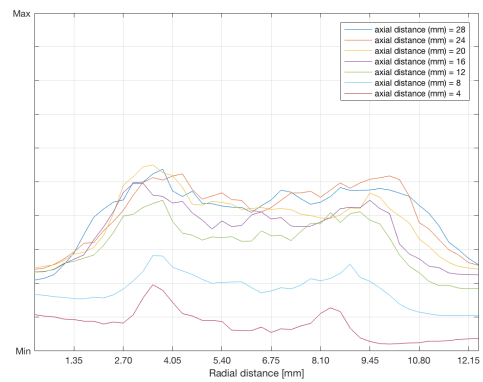
(a)  $P_c = 10$  bar,  $OF = 4.4$



(b)  $P_c = 10$  bar,  $OF = 5.2$



(c)  $P_c = 10$  bar,  $OF = 6.0$



(d)  $P_c = 10$  bar,  $OF = 6.8$

**Figure 5.7:** OH\* Emission trends at different axial distances and a chamber pressure of 10 bar

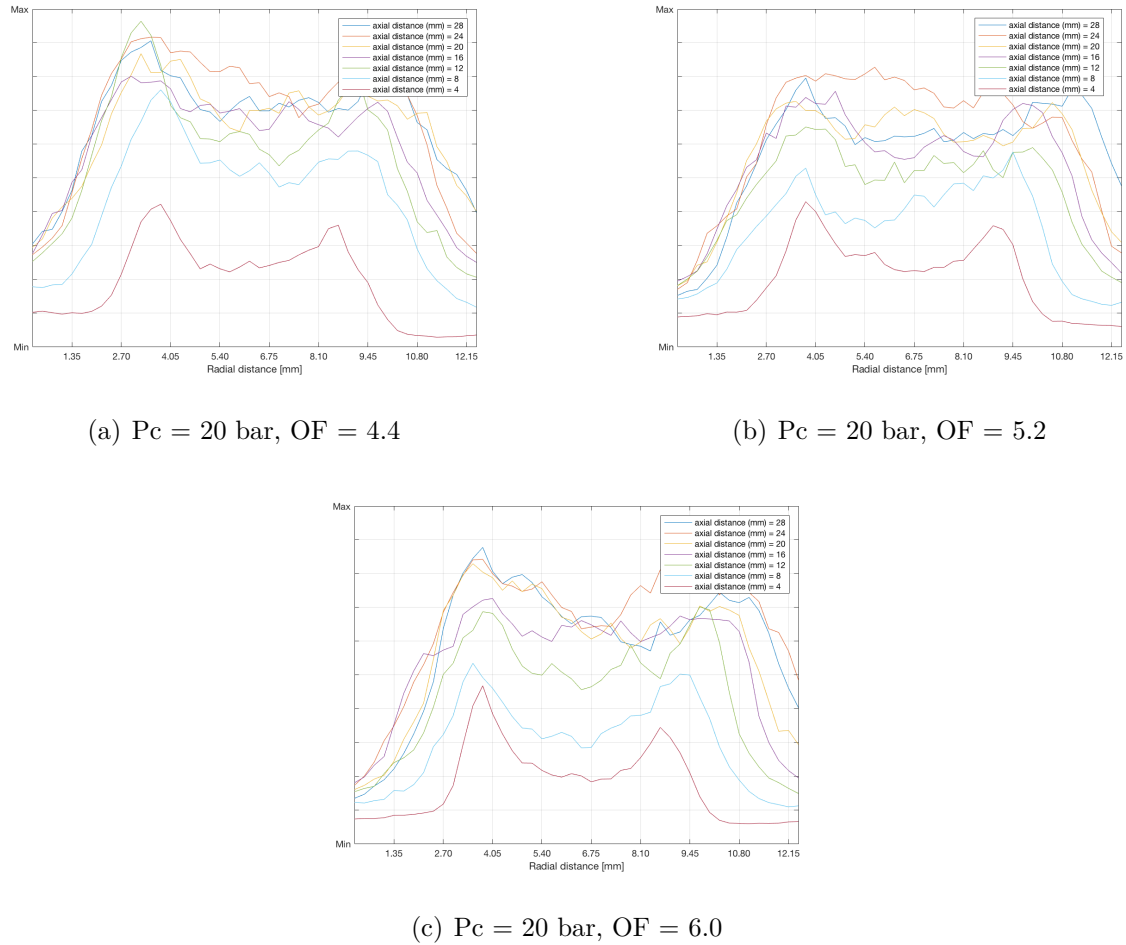


**Figure 5.8:** OH\* Emission trends at different axial distances and a chamber pressure of 20 bar

The cylindrical-like flame envelops the oxidizer jet in the first part of the visible access and, after an axial distance of about 2-3 times the GOX inlet internal diameter  $d_i$ , the flame slightly expands radially and diverges from the combustion chamber centerline to the combustor walls. This characteristic flame expansion can be explained by the decreasing shear forces of the coflowing hydrogen on the oxygen jet at a certain distance from the injector face. The spreading is found to be slightly sensitive to VR (and J) variation and pressure variation.

Increasing the combustion chamber pressure at constant VR (and J) results in a widening of the flame and a slight increasing of the spreading angle. It also can be seen from these images that an increasing oxygen injection velocity (increasing OF and, thus, decreasing VR and J) leads to a constriction of the flame and a decreasing spreading angle. A thinner plume is visible increasing oxidizer-to-fuel ratio, the now predominant oxygen stream carrying the flame downstream along the combustor. A non- or low-emitting zone

along the chamber axis is representative of the presence of the oxidizer jet where no combustion takes place [33].

The color scale has been normalized with the maximum emission intensity for each operating point. It is evident from Fig 5.5 that the total flame emission intensity decreases with decreasing chamber pressure. With a reduction of the combustion chamber pressure from 20 to 10 bar, the OH emission intensity drops by about 40-50%.

For both the pressures tested in combustion chamber, the flame has a common trend with the increase of mixture ratio. It results a flame front closer to the axis and away from the chamber walls, to the increase of the mixture ratio. This trend is explained by the fact that as the OF increases, the mass flow rate of oxygen, the central flow, and therefore its velocity, also increases. A flame with an higher oxygen velocity (VR and J decreasing) recalls the flow of the hydrogen, external and concentric, towards the inside of the flame. This causes the flame to crush on the horizontal axis and to move away from the walls of the combustion chamber. It seems that for lower ROF, for which the external hydrogen jet is faster, the flame fluctuations are more pronounced when compared to higher ROF, for which the internal oxygen jet is faster and fluctuations are mainly predominated in the shear layer between the propellants. Besides, decreasing mixture ratio ROF and then increasing the injection velocity ratio VR and the momentum flux ratio J (at constant chamber pressure) slightly increases the OH emission intensity. This is due to the fact that an increase in the velocity of hydrogen and therefore of the velocity ratio and momentum flux ratio, leads to an increase in the shear force between the two flows and therefore to an improvement in the mixing. The emissions are therefore higher for smaller ROFs in accordance with the previous experiments. This trend can be noticed more for the cases at 20 bar since the normalization was performed for the case at 20 bar, the variations of test emissions at 10 bar are less perceptible. But as regards the cases at 10 bar this trend can be observed thanks to the volume of the flame that appears gradually smaller with the increase of the mixture ratio. Therefore, with the same emission values achieved, emissions are greater where the volume is larger. Even for the case at 20 bar with OF = 6.0, the flame appears brighter than in the case 20 bar with OF = 5.2, but the volume is much lower, so even in this case the emissions are greater for the case with lower mixture ratio. A proof of the fact that emissions are higher for smaller mixture ratios is shown in the following graphs (Figure 5.9 and Figure 5.10), showing the trend of emissions along the horizontal main axis. Each curve represents the trend along the x-axis of the intensity when the mixture ratio changes, and each point represents the average intensity between all the points along y-axis with equal x-abscissae. It is shown how the intensity grows roughly in the right half of each image, where there is a concentration of the reaction process, then as the axial distance increases. Comparing the trends at the same pressure,

note how the intensities reached in the right half of each photo are gradually lower as the mixture ratio increases, except for the trend in the extreme part to the right in the case 10 bar, where the curves have the opposite trend. Further confirmation can be obtained from the graphs in the Figure 5.7 and 5.8 by observing the values achieved in the various cases. On average, once the pressure is set, the emission values reached are gradually higher for lower mixture ratios.

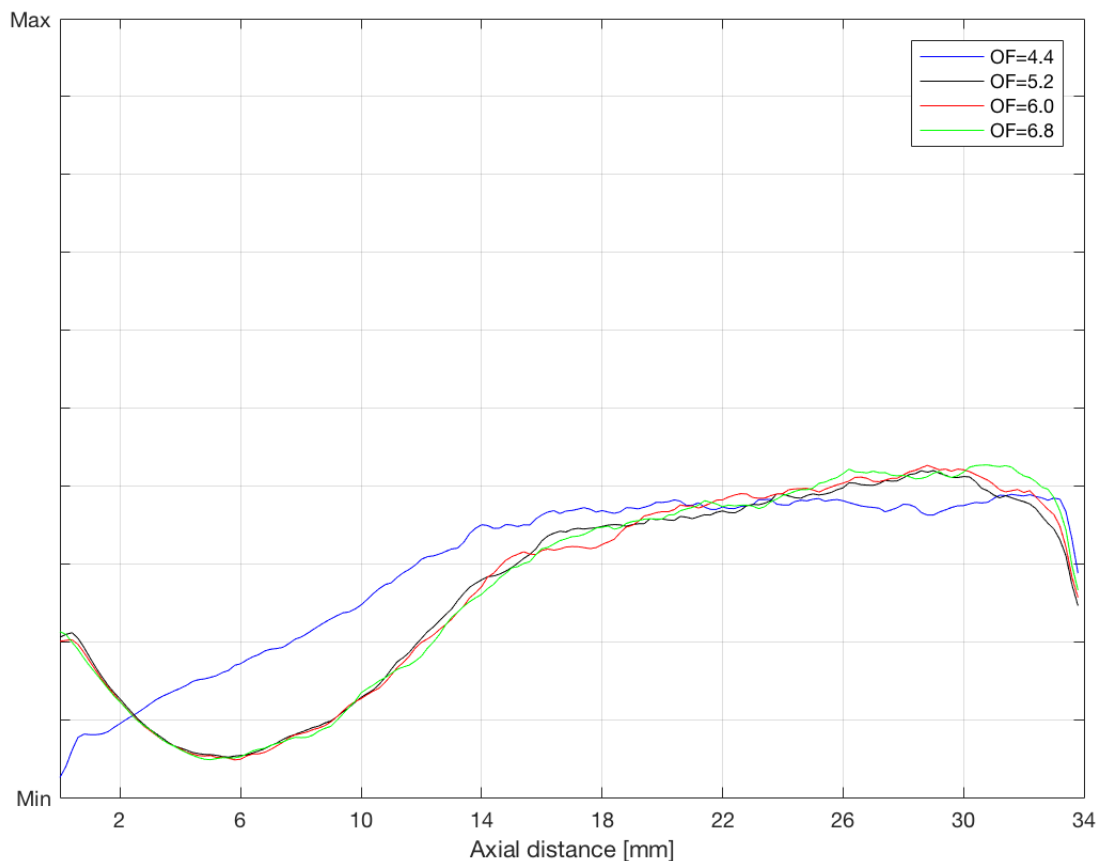


**Figure 5.9:** OH\* Emission trends along horizontal main axes at a chamber pressure of 10 bar

It seems that the flame is moved downstream of the faceplate with the increase of ROF what consequently results in lower temperature values and heat flux in the near injector area. According to Perakis et al [28], where the initial mixing effect is negligible, the energy release increases, the heat flux and temperature values rise and become higher for ROFs, which are closer to the stoichiometric condition.

Although the emission is very low in the centerline of the flame, the emission intensity in all pictures of Figure 5.5 and 5.6 does not decrease to very low values in that region. That is because emission imaging is a line-of-sight technique and thus light is collected from in

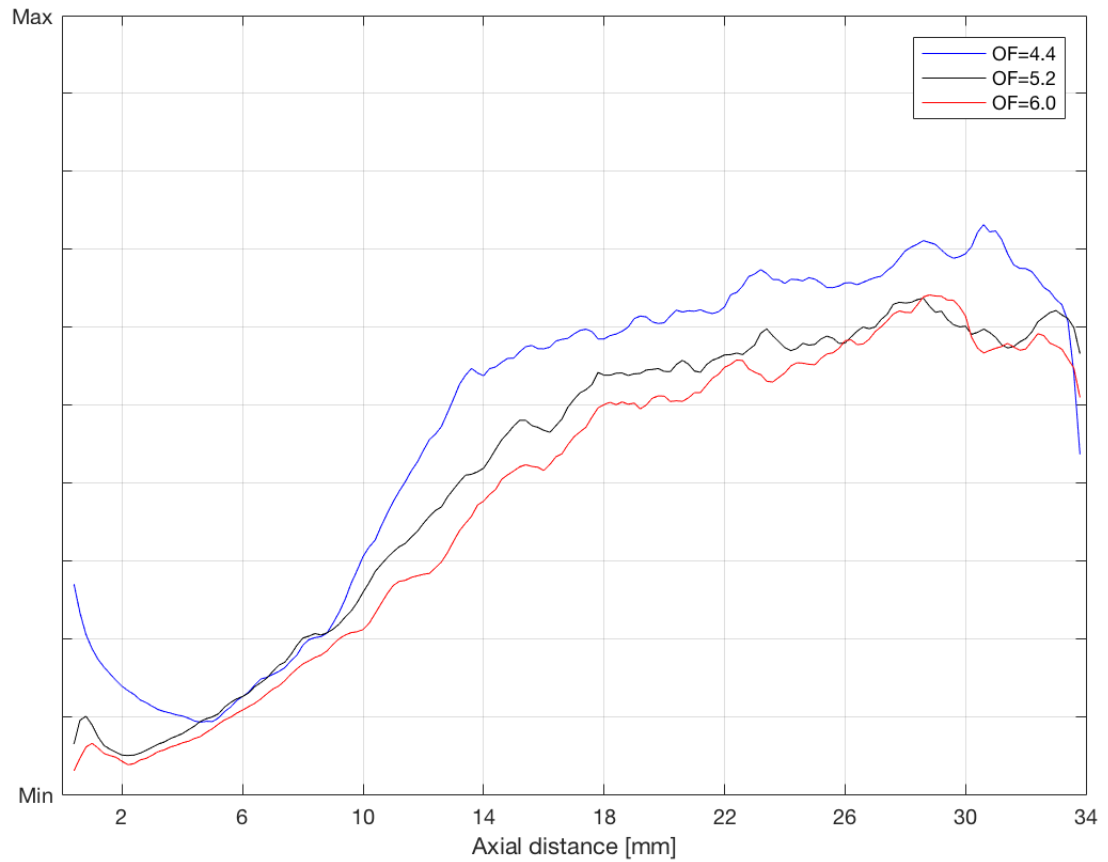


**Figure 5.10:** OH\* Emission trends along horizontal main axes at a chamber pressure of 20 bar

front of and behind the focal plane of the camera lens. In future investigations, an Abel transform can be applied in order to compare these experimental results with numerical simulations.

Small differences on the distance from the flame front to the combustion chamber wall was observed for different ROFs, and the flame seems to move in a more downstream position for higher ROF.

## Chapter 6

# Conclusions

A rectangular inner cross section combustion chamber with optical access has been assembled and tested at a pressure level of 10 and 20 bar with variable mixture ratio from 4.4 to 6.0 (6.8 only for 10 bar test case). A gaseous hydrogen/oxygen single-element shear coaxial injector is used. All investigations, in particular flame emission, flame structure and its anchoring, have been studied through a non-invasive optical diagnostic method. To detect the flame anchoring near the oxygen post tip, a Digital Camera from Toshiba (USB Camera) has been used. Furthermore, to characterize the flame front and the combustion process, it was necessary to detect hydroxyl radicals ( $\text{OH}^*$ ) emission. Flame emission can be passively estimated from chemiluminescence technique. In this case an iCCD Camera Flame Star 2, equipped with a filter, has registered the light emitted from the excited OH, denoted  $\text{OH}^*$ , when they return to ground state. Due to the nature of this diagnostic, the measurements may not have been carried out under the same conditions. Optical measurements are always subjected to positioning errors and influenced by external factors, therefore a good post-processing work is necessary.

In this case, a non-homogeneous brightness characterized all the images collected through the tests with both cameras. This was due to an intrinsic error of the cameras, added to the fact that the environmental conditions in which the tests took place did not favor a homogeneous illumination of the optical access. It was therefore necessary to develop a matlab code capable of correcting the images collected, creating the most homogeneous possible background lighting conditions. In this way it was possible to analyze and compare the measurements under the same lighting conditions. After correcting the images, it was possible to proceed with the actual analysis of the results.

First of all the anchoring of the flame was analyzed. A sequence of acquired instantaneous images taken during a time range of  $100 \mu\text{s}$  have been observed. When the igniter is activated in the middle of the combustion chamber the flame moves upstream. After initial oscillations, the flame anchors and gets slowly brighter with time. These initial

fluctuations in the axial direction occur at a distance not longer than 20 mm from the faceplate.

It was then proceeded to analyze the emissions of  $\text{OH}^*$  radicals to find out how the hydrogen / oxygen combustion develops and the behavior of the flame produced when the pressure and mixture ratio vary. For both pressures levels tested, with pressure fixed and increasing mixture ratio, it results a flame front closer to the axis and away from the chamber walls. But the increase in the mixture ratio also leads to a lower volume of  $\text{OH}^*$  emissions. Besides, it seems that the flame is moved downstream of the faceplate with the increase of ROF. With the same mixture ratio value, reducing combustion chamber pressure from 20 to 10 bar, the OH emission intensity drops by about 40-50%.

In conclusion comparing this results with the collected data concerning a methane / oxygen combustion, they seemed coherent (to rely on the thesis produced by Pasquale Difficile, to have a direct comparison with an oxygen / methane combustion). Further investigations will be necessary in the future to better classify the flame behavior in the case of a hydrogen / oxygen combustion, perhaps by performing a recess investigation of the flame and then observing how it behaves accordingly. Naturally, the knowledge about this type of combustion is greater than a methane / oxygen combustion. However, there remains the need for comparison parameters in order to develop a correct evaluation, and for this reason it will be necessary in future to carry out new hydrogen test campaigns.



# Bibliography

- [1] BROCKHINKE, A. ; KRUGER, J. ; HEUSING, M. ; LETZGUS, M.: *Measurement and simulation of rotationally-resolved chemiluminescence spectra in flames*. Applied Physics B: Lasers and Optics, 2012
- [2] CELANO, M. P. ; KIRCHBERGER, C. ; SILVESTRI, S. ; SCHLIEBEN, G. ; HAIDN, O. J.: *Characterization of a GOX/GCH<sub>4</sub> single element combustion chamber / Institute for Flight Propulsion (LFA), Technische Universität München (TUM)*. 2014. – Forschungsbericht
- [3] DIEDERICHSEN, J. ; WOLFHARD, H. G.: *Spectrographic Examination of Gaseous Flames at High Pressure*. Proceedings of the Royal Society of London, 1956
- [4] DIFFICILE, Pasquale: *Performance and Emission Imaging of a Coaxial Single Element GO<sub>2</sub>/GCH<sub>4</sub> Rocket Combustion Chamber*, Technische Universität München, Diplomarbeit, 2018
- [5] ESA, European Space A.: *Solid and Liquid Fuel Rockets*. [http://www.esa.int/Education/Solid\\_and\\_liquid\\_fuel\\_rockets4/%28print%29](http://www.esa.int/Education/Solid_and_liquid_fuel_rockets4/%28print%29). Version: 2018
- [6] FIALA, Thomas: *Radiation from High Pressure Hydrogen-Oxygen Flames and its Use in Assessing Rocket Combustion Instability*, Technische Universität München, Institut für Energietechnik, Diss., 2015
- [7] FINKELNBURG, W.: *Kontinuierliche Spektren*. Springer Berlin Heidelberg, 1938
- [8] GAYDON, A. G.: *The Spectroscopy of Flames*. 2nd edition. Chapman and Hall, 1974
- [9] GAYDON, A. G. ; WOLFHARD, H. G.: *Predissociation in the Spectrum of OH; the Vibrational and Rotational Intensity Distribution in Flames*. Proceedings of the Royal Society of London, 1951
- [10] GAYDON, A. G. ; WOLFHARD, H. G.: *The Spectrum-Line Reversal Method of Measuring Flame Temperature*. Proceedings of the Physical Society, 1952

- 
- [11] GORDON, S. ; MCBRIDE, B. J.: *Computer Program for Calculation of Complex Chemical Equilibrium*. NASA, 1994
- [12] HALL, J. M. ; PETERSEN, E. L.: *An optimized kinetics model for OH chemiluminescence at high temperatures and atmospheric pressures*. International Journal of Chemical Kinetics, 2006
- [13] HIDAKA, Y. ; TAKAHASHI, S. ; KAWANO, H. ; SUGA, M. ; GARDINER, W. C.: *Shock-tube measurement of the rate constant for excited hydroxyl formation in the hydrogen-oxygen reaction*. Journal of Physical Chemistry, 1982
- [14] HIGGINS, B. ; MCQUAY, M. ; LACAS, F. ; ROLON, J. ; DARABIHA, N. ; CANDEL, S.: *Systematic measurements of OH chemiluminescence for fuel-lean, high-pressure, premixed, laminar flames*. Fuel, 2001
- [15] KATHROTIA, T. ; FIKRI, M. ; BOZKURT, M. ; HARTMANN, M. ; RIEDEL, U. ; SCHULZ, C.: *Study of the H+O+M reaction forming OH\*: Kinetics of OH\* chemiluminescence in hydrogen combustion systems*. Combustion and Flame, 2010
- [16] KLIMENKO, D. ; SMITH, J. ; SUSLOV, D.: *Flame-Emission Spectroscopy at High Pressure Combustion in Combustor / DLR Lampoldshausen*. 2004. – Forschungsbericht
- [17] KOIKE, T. ; MORINAGA, K.: *Further Studies of the Rate Constant for Chemical Excitation of OH in ShockWaves*. Bulletin of the Chemical Society of Japan, 1982
- [18] KOIKE, T. ; MORINAGA, K.: *Further Studies of the Rate Constant for Chemical Excitation of OH in ShockWaves*. Bulletin of the Chemical Society of Japan, 1982
- [19] LAUER, Rolf Martin W.: *Determination of the Heat Release Distribution in Turbulent Flames by Chemiluminescence Imaging*, Technische Universität München, Institut für Energietechnik, Diss., 2011
- [20] LEO, M. D. ; SAVELIEV, A. ; KENNEDY, L. A. ; ZELEPOUGA, S. A.: *OH and CH luminescence in opposed flow methane oxy-flames*. Combustion and Flame, 2007
- [21] LIVEING, G. D. ; DEWAR, J.: *On the Influence of Pressure on the Spectra of Flames*. Proceedings of the Royal Society of London, 1890
- [22] MAVRODINEANU, R. ; BOITEUX, H.: *Flame Spectroscopy*. John Wiley and Sons, 1965

- [23] MODEST, M. F.: *Radiative Heat Transfer*. 3rd edition. Elsevier, 2013
- [24] NAROM, Andoya Space C.: *The engine types: solid, liquid and hybrid... and a fourth.* <https://www.narom.no/undervisningsressurser/sarepta/rocket-theory/rocket-engines/the-engine-types-solid-liquid-and-hybrid-and-a-fourth/>. Version: 2017
- [25] NASA: *Liquid Hydrogen-The Fuel of Choice for Space Exploration.* [https://www.nasa.gov/topics/technology/hydrogen/hydrogen\\_fuel\\_of\\_choice.html](https://www.nasa.gov/topics/technology/hydrogen/hydrogen_fuel_of_choice.html). Version: 2010
- [26] NORI, V. N.: *Modeling and Analysis of Chemiluminescence Sensing for Syngas, Methane and Jet-A Combustion*, Georgia Institute of Technology, Diss., 2008
- [27] PADLEY, P. J.: *The origin of the blue continuum in the hydrogen flame.* Trans. Faraday Soc, 1960
- [28] PERAKIS, F. ; CELANO, M. P. ; HAIDN, O. J.: Heat flux and temperature evaluation in a rectangular multi-element GOX/GCH<sub>4</sub> combustion chamber using an inverse heat conduction method. In: *7th European Conference for Aerospace Sciences* (2017)
- [29] RUSH, John C.: *The Image Processing Handbook*. Sixth edition. United States of America : CRC Press, Taylor and Francis Group, 2011
- [30] SCHEFER, R. ; KULATILAKA, W. ; PATTERSON, B. ; SETTERSTEN, T.: *Visible emission of hydrogen flames.* Combustion and Flame, 2009
- [31] SUTTON, G. P. ; BIBLARZ, O.: *Rocket Propulsion Elements*. John Wiley and Sons, 2001
- [32] VANPEE, M. ; MAINIERO, R.: *The spectral distribution of the blue hydrogen flame continuum and its origin in hydrogen-nitric oxide flames.* Combustion and Flame, 1979
- [33] WINTER, F. ; CELANO, M. P. ; SILVESTRI, S. ; SCHLIEBEN, G. ; HAIDN, O. J.: High-speed and Emission Imaging of a Coaxial Single Element GOX/GCH<sub>4</sub> Rocket Combustion Chamber. In: *7th European Conference for Aerospace Sciences* (2017)

## Appendix A

# Matlab Code

### A.1 ICCD Camera

```
1 clear all;
2 clc;
3 close all;
4 %%% IMPORT IMAGE(*.txt) AND PROCESS IMAGE %%%
5
6 FileSystemPath= dir( fullfile (TXTDir, '*.txt') );
7 [tmp ind]=sort ({ FileSystemPath.date } );
8 FileSystemPath=FileSystemPath(ind);
9 cd(TXTDir)
10
11 % INSERT PIECE OF CODE FROM PASQUALE DIFFICILE THESIS %
12
13 % v2=v1(98:143,102:271); % tcw-10-44-20-20-2
14 %v2=v1(96:141,102:266); % tcw-10-52-20-20-1
15 %v2=v1(96:141,102:266); % tcw-10-60-20-20-6
16 %v2=v1(97:142,103:274); % tcw-10-68-20-20-8
17 %v2=v1(97:142,106:275); % tcw-20-44-20-20-1
18 %v2=v1(92:137,85:253); % tcw-20-52-20-20-1
19 v2=v1(92:142,86:253); % tcw-20-60-20-20-5
20
21 size=size(v2);
22 v2=v2/6681.7;
23 figure(3)
```

```

24 set (figure (3), 'Position', [100 100 450 150])
25 IMAGE=imagesc (v2);
26 colormap (jet (256))
27 %limits=[250 5228]; %LIMIT OF METHANE
28 limits=[0 1]; %LIMIT OF HYDROGEN
29 colorbar;
30 colorbar ('Ticks', [0,1], 'TickLabels', {'Min', 'Max'})
31 %limits=[0 2000];
32 caxis (limits)
33
34 set (gca, 'xDir', 'reverse');
35 title (sprintf ('CUTTED AND REVERSED IMAGE WITH UNIFIED COLOR
36 SCALE'))
37 saveas (figure (3), [TXTDir '\AverageWindowed'], 'fig')
38 saveas (figure (3), [TXTDir '\AverageWindowed'], 'png')
39
40 if flag==1
41 sigma = 10; % chosen by visual inspection
42 B = imgaussfilt (v2, sigma); %solo per calibrazione
43 save ('/Users/Graziano/Documents/MATLAB/Script ICCD/
44 Codice_DEFINITIVO.mat', 'B'); %solo per calibrazione
45 else
46 load ('/Users/Graziano/Documents/MATLAB/Script ICCD/
47 Codice_DEFINITIVO.mat', 'B'); % solo per fiamma
48 end
49 figure (11)
50 set (figure (11), 'Position', [100 100 450 150])
51 Back=imagesc (B);
52 colormap (jet (256))
53 %limits=[250 5228]; %LIMIT OF METHANE
54 limits=[250 5723]; %LIMIT OF HYDROGEN
55 colorbar;
56 colorbar ('Ticks', [250,5723], 'TickLabels', {'Min', 'Max'})
57 %limits=[0 2000];
58 caxis (limits)
59 set (gca, 'xDir', 'reverse');

```

```
57 title(sprintf('BACKGROUND IMAGE WITH SIGMA = 10'))
58 saveas(figure(11),[TXTDir '\Background'], 'fig')
59 saveas(figure(11),[TXTDir '\Background'], 'png')
60
61 I2=imsubtract(v2,(B));
62
63 figure(12)
64 set(figure(12), 'Position', [100 100 450 150])
65 Sub=imagesc(I2);
66 colormap(jet(256))
67 %limits=[250 5228]; %LIMIT OF METHANE
68 limits=[250 5723]; %LIMIT OF HYDROGEN
69 colorbar;
70 colorbar('Ticks',[250,5723], 'TickLabels',{ 'Min', 'Max' })
71 %limits=[0 2000];
72 caxis(limits)
73 set(gca, 'xDir', 'reverse');
74 title(sprintf('RESULT OF SUBTRACTING THE BACKGROUND FROM THE
75 ORIGINAL IMAGE'))
76 saveas(figure(12),[TXTDir '\Subtracted'], 'fig')
77 saveas(figure(12),[TXTDir '\Subtracted'], 'png')
78
79 c=mean(mean(B));
80 I3=I2+c;
81
82 Min=min(min(I3))
83 Max=max(max(I3))
84
85     if Min<0
86         I3=I3+abs(Min);
87         max(max(I3))
88         min(min(I3))
89     else
90     end
91
```

```

92 I3=I3/6681.7; %for hydrogen
93
94 figure(10)
95 set(figure(10), 'Position', [100 100 450 150])
96 im=imagesc(I3);
97 colormap(jet(256))
98 %limits=[250 5228]; %LIMIT OF METHANE
99 %limits=[250 5723]; %LIMIT OF HYDROGEN
100 limits=[0 1];
101 colorbar;
102 colorbar('Ticks',[0,1], 'TickLabels',{ 'Min', 'Max'})
103 %limits=[0 2000];
104 caxis(limits)
105 set(gca, 'xDir', 'reverse');
106 xticks([20 40 60 80 100 120 140 160])
107 xticklabels({'160', '140', '120', '100', '80', '60', '40', '20'})
108 % title(sprintf('SHADING CORRECTED IMAGE WITH UNIFIED COLOR
109           SCALE'))
109 saveas(figure(10), [TXTDir '\SHADINGCorrectedImage'], 'fig')
110 saveas(figure(10), [TXTDir '\SHADINGCorrectedImage'], 'png')
111
112
113 %%%%%%%%%% Brightness %%%%%%%%%%
114 figure(4)
115 plot(mean(d2))
116 axis([0 size(2) 0 1])
117 set(gca, 'xDir', 'reverse');
118 grid on
119 title(sprintf('ORIGINAL IMAGE Brightness'));
120 saveas(figure(4), [TXTDir '\ORIGINAL IMAGE Brightness'], 'fig')
121 saveas(figure(4), [TXTDir '\ORIGINAL IMAGE Brightness'], 'png')
122
123 figure(8)
124 plot(mean(I3))
125 axis([0 size(2) 0 1])
126 set(gca, 'xDir', 'reverse');

```

```

127 xticks([0 20 40 60 80 100 120 140 160])
128 xticklabels({'160','140','120','100','80','60','40','20','0'})
129 yticks([0 0.1 0.2 0.3 0.4 0.5 0.6 0.7 0.8 0.9 1])
130 yticklabels({'Min','','',' ',' ',' ',' ',' ',' ',' ',' ','Max'})
131 grid on
132 %title(sprintf('CORRECTED IMAGE Brightness'));
133 saveas(figure(8),[TXtDir '\CORRECTED IMAGE Brightness'],'fig')
134 saveas(figure(8),[TXtDir '\CORRECTED IMAGE Brightness'],'png')
135
136 %%%%%%%%%% Edge detection %%%%%%%%%%
137 figure(5)
138 BW_canny = edge(I3, 'canny', 0.21);
139 BW_canny_inv = imcomplement(BW_canny);
140 imshow(BW_canny_inv);
141 set(gca, 'xDir', 'reverse');
142 title(sprintf('Edge detection'));
143 saveas(figure(5),[TXtDir '\Edge detection'],'fig')
144 saveas(figure(5),[TXtDir '\Edge detection'],'png')
145
146 %%%%%%%%%% Plot in different axial distances
147 %%%%%%%%%%
148 figure(6)
149 set(figure(6), 'Position', [100 100 540 400])
150 graph1 = plot(I3(:,[10,30,50,70,90,110,130]));
151 axis([1 size(1) 0 1])
152 % set(graph1, 'LineWidth', 2);
153 legend('axial distance = 130', 'axial distance = 110', 'axial
154         distance = 90', 'axial distance = 70', 'axial distance = 50', '
155         axial distance = 30', 'axial distance = 10');
156 yticks([0 0.1 0.2 0.3 0.4 0.5 0.6 0.7 0.8 0.9 1])
157 yticklabels({'Min','','',' ',' ',' ',' ',' ',' ',' ',' ','Max'})
158 grid on
159 saveas(figure(6),[TXtDir '\Average Axial distances'],'fig')
160 saveas(figure(6),[TXtDir '\Average Axial distances'],'png')

```

## A.2 Digital Camera

```

1 clear all;
2 clc;
3 close all;
4 %%% IMPORT IMAGE(*.txt) AND PROCESS IMAGE %%%
5
6 FileSystemPath= dir(fullfile(TXTDir, '*.txt'));
7 [tmp ind]=sort({FileSystemPath.date});
8 FileSystemPath=FileSystemPath(ind);
9 cd(TXTDir)
10
11 % INSERT PIECE OF CODE FROM PASQUALE DIFFICILE THESIS %
12
13 size=size(H1);
14
15 figure(3)
16 set(figure(3), 'Position', [100 100 450 150])
17 IMAGE=imagesc(H1);
18 colormap('gray')
19 colorbar;
20 if flag==0
21 %limits=[0 2]; %LIMIT OF METHANE
22 limits=[0 2]; %LIMIT OF HYDROGEN
23 colorbar('Ticks',[0,2], 'TickLabels',{'Min','Max'})
24 caxis(limits)
25 else
26 limits=[0 max(max(H1))];
27 colorbar('Ticks',[0,max(max(H1))], 'TickLabels',{'Min','Max'})
28 caxis(limits)
29 end
30 set(gca, 'xDir', 'reverse');
31 title(sprintf('CUTTED AND REVERSED IMAGE WITH UNIFIED COLOR
    SCALE'))
32 saveas(figure(3),[TXTDir '\AverageWindowedBW'], 'fig')
33 saveas(figure(3),[TXTDir '\AverageWindowedBW'], 'png')

```

```
34
35 if flag==1
36 sigma = 10; % chosen by visual inspection
37 background = imgaussfilt(H1,sigma); %solo per calibrazione
38 save('/Users/Graziano/Documents/MATLAB/Script ICCD/Codice_Prova2
    .mat','background'); %solo per calibrazione
39 else
40 load('/Users/Graziano/Documents/MATLAB/Script ICCD/Codice_Prova2
    .mat','background'); % solo per fiamma
41 end
42 figure(11)
43 set(figure(11), 'Position', [100 100 450 150])
44 Back=imagesc(background);
45 colormap('gray')
46 colorbar;
47 limits=[0 max(max(background))];
48 colorbar('Ticks',[0,max(max(background))], 'TickLabels',{ 'Min', '
    Max'})
49 caxis(limits)
50 set(gca, 'xDir', 'reverse');
51 title(sprintf('BACKGROUND IMAGE WITH SIGMA = 10'))
52 saveas(figure(11), [TXTDir '\BackgroundBW'], 'fig')
53 saveas(figure(11), [TXTDir '\BackgroundBW'], 'png')
54
55 I2 = H1./(background);
56
57 figure(12)
58 set(figure(12), 'Position', [100 100 450 150])
59 Sub=imagesc(I2);
60 colormap('gray')
61 if flag==0
62 %limits=[0 2]; %LIMIT OF METHANE
63 limits=[0 2]; %LIMIT OF HYDROGEN
64 colorbar('Ticks',[0,2], 'TickLabels',{ 'Min', 'Max'})
65 caxis(limits)
66 else
```

```

67 limits=[0 max(max(I2))];
68 colorbar('Ticks',[0,max(max(I2))],'TickLabels',{'Min','Max'})
69 caxis(limits)
70 end
71 caxis(limits)
72 set(gca,'xDir','reverse');
73 title(sprintf('RESULT OF DIVIDING THE BACKGROUND FROM THE
    ORIGINAL IMAGE'))
74 saveas(figure(12),[TXTDir '\SubtractedBW'],'fig')
75 saveas(figure(12),[TXTDir '\SubtractedBW'],'png')
76
77 c=mean(mean(background));
78 I3=I2*c;
79
80 figure(10)
81 set(figure(10),'Position',[100 100 450 150])
82 im=imagesc(I3);
83 colormap('gray')
84 colorbar;
85 if flag==0
86 %limits=[0 2]; %LIMIT OF METHANE
87 limits=[0 2]; %LIMIT OF HYDROGEN
88 colorbar('Ticks',[0,2],'TickLabels',{'Min','Max'})
89 caxis(limits)
90 else
91 limits=[0 max(max(I3))];
92 colorbar('Ticks',[0,max(max(I3))],'TickLabels',{'Min','Max'})
93 caxis(limits)
94 end
95 set(gca,'xDir','reverse');
96 title(sprintf('SHADING CORRECTED IMAGE WITH UNIFIED COLOR SCALE'
    ))
97 saveas(figure(10),[TXTDir '\SHADINGCorrectedImageBW'],'fig')
98 saveas(figure(10),[TXTDir '\SHADINGCorrectedImageBW'],'png')
99
100

```

```
101 %%%%%%%%%% Brightness %%%%%%%%%%
102 figure(4)
103 plot(mean(H1))
104 axis([0 size(2) 0 1])
105 set(gca, 'xDir', 'reverse');
106 title(sprintf('ORIGINAL IMAGE Brightness'));
107 saveas(figure(4), [TXTDir '\ORIGINAL IMAGE BrightnessBW'], 'fig')
108 saveas(figure(4), [TXTDir '\ORIGINAL IMAGE BrightnessBW'], 'png')
109
110 figure(8)
111 plot(mean(I3))
112 axis([0 size(2) 0 1])
113 set(gca, 'xDir', 'reverse');
114 title(sprintf('CORRECTED IMAGE Brightness'));
115 saveas(figure(8), [TXTDir '\CORRECTED IMAGE BrightnessBW'], 'fig')
116 saveas(figure(8), [TXTDir '\CORRECTED IMAGE BrightnessBW'], 'png')
```

## **Appendix B**

# **Experimental Data**

The following pages show the calculations of the velocity ratios and momentum flux ratios, performed by means of experimental temperature and pressure measurements. The density has been defined thanks to the molar mass and the constant of the perfect gases, through gas perfect law. Besides, thanks to the experimental measurements of the mass flow rate and the knowledge of the injector geometry, it was possible to calculate the volume flow rate and therefore the injection velocity of the propellants.

R= 8,314	J/K·mol
Mo= 0,016	kg/mol
Mh= 0,001	kg/mol
Ao= 1,2566E-05	m <sup>2</sup>
Alh= 8,6394E-06	m <sup>2</sup>

Pc = 10 bar

	Idrogeno	Ossigeno
OF=4.4	PC0 = 961520 TM3 = 287,9746 ro = 0,401600383 mdoH = 0,0043 vdoH = 0,010707161 v = 1239,343721	PC0 = 961520 TO3 = 291,3294 ro = 6,35161214 mdoH = 0,0187 vdoH = 0,00294413 v = 234,286774
	VR = J =	VR = J =

	Idrogeno	Ossigeno
OF=6.0	PC0 = 965610 TM3 = 284,7607 ro = 0,40786053 mdoH = 0,0036 vdoH = 0,0082655 v = 1021,66438	PC0 = 965610 TO3 = 287,5529 ro = 6,46240193 mdoH = 0,0209 vdoH = 0,00323409 v = 257,360835
	VR = J =	VR = J =

	Idrogeno	Ossigeno
OF=5.2	PC0 = 977760 TM3 = 285,6153 ro = 0,411756798 mdoH = 0,004 vdoH = 0,009714472 v = 1124,440833	PC0 = 977760 TO3 = 289,0666 ro = 6,50945029 mdoH = 0,0201 vdoH = 0,00308782 v = 245,720776
	VR = J =	VR = J =

	Idrogeno	Ossigeno
OF=6.8	PC0 = 952380 TM3 = 284,3348 ro = 0,40287492 mdoH = 0,0033 vdoH = 0,00819113 v = 948,115275	PC0 = 952380 TO3 = 286,7132 ro = 6,39252656 mdoH = 0,0218 vdoH = 0,00341023 v = 271,377657
	VR = J =	VR = J =

Pc = 20 bar

	Idrogeno	Ossigeno
OF=4.4	PC0 = 1977100 TM3 = 285,1157 ro = 0,834060364 mdoH = 0,0086 vdoH = 0,010311004 v = 1193,488947	PC0 = 1977100 TO3 = 288,1132 ro = 13,2061262 mdoH = 0,0384 vdoH = 0,00290774 v = 231,39071
	VR = J =	VR = J =

	Idrogeno	Ossigeno
OF=6.0	PC0 = 2041770 TM3 = 290,3552 ro = 0,84579904 mdoH = 0,0072 vdoH = 0,00851266 v = 985,332346	PC0 = 2041770 TO3 = 292,4668 ro = 13,4350785 mdoH = 0,0402 vdoH = 0,00299217 v = 238,109093
	VR = J =	VR = J =

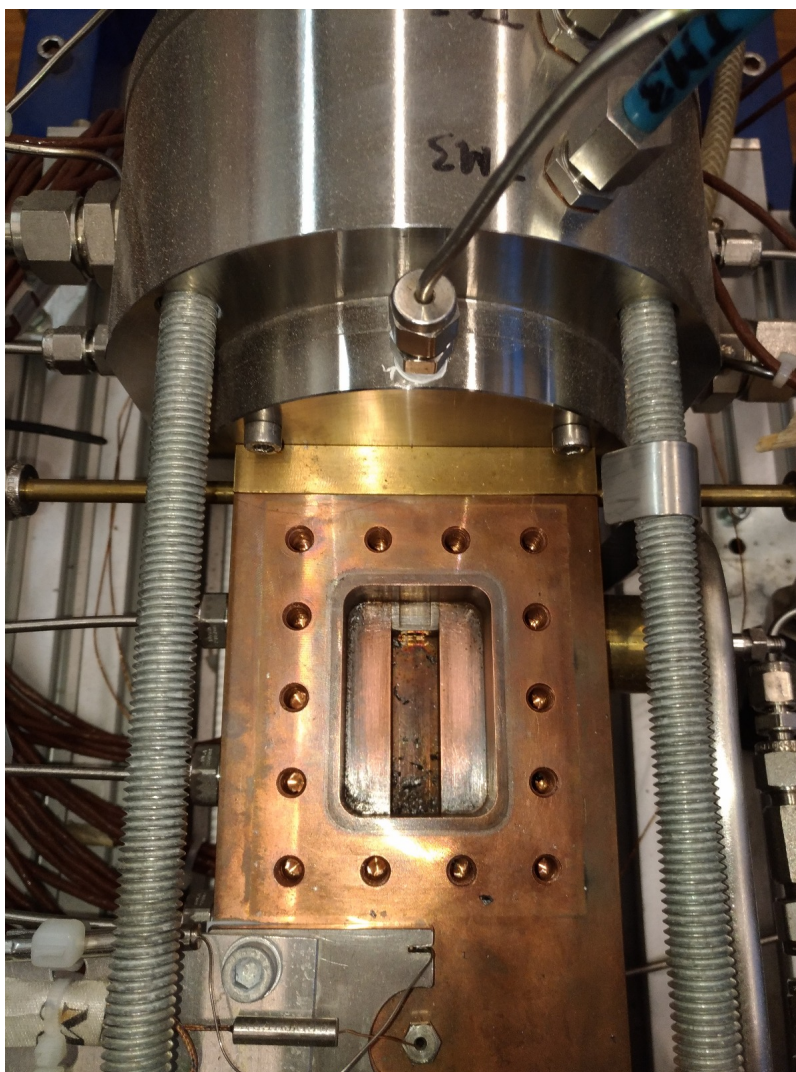
	Idrogeno	Ossigeno
OF=5.2	PC0 = 1987060 TM3 = 289,0749 ro = 0,82678117 mdoH = 0,0077 vdoH = 0,009313226 v = 1077,997074	PC0 = 1987060 TO3 = 289,7847 ro = 13,1960968 mdoH = 0,0381 vdoH = 0,00288722 v = 229,757459
	VR = J =	VR = J =

## Appendix C

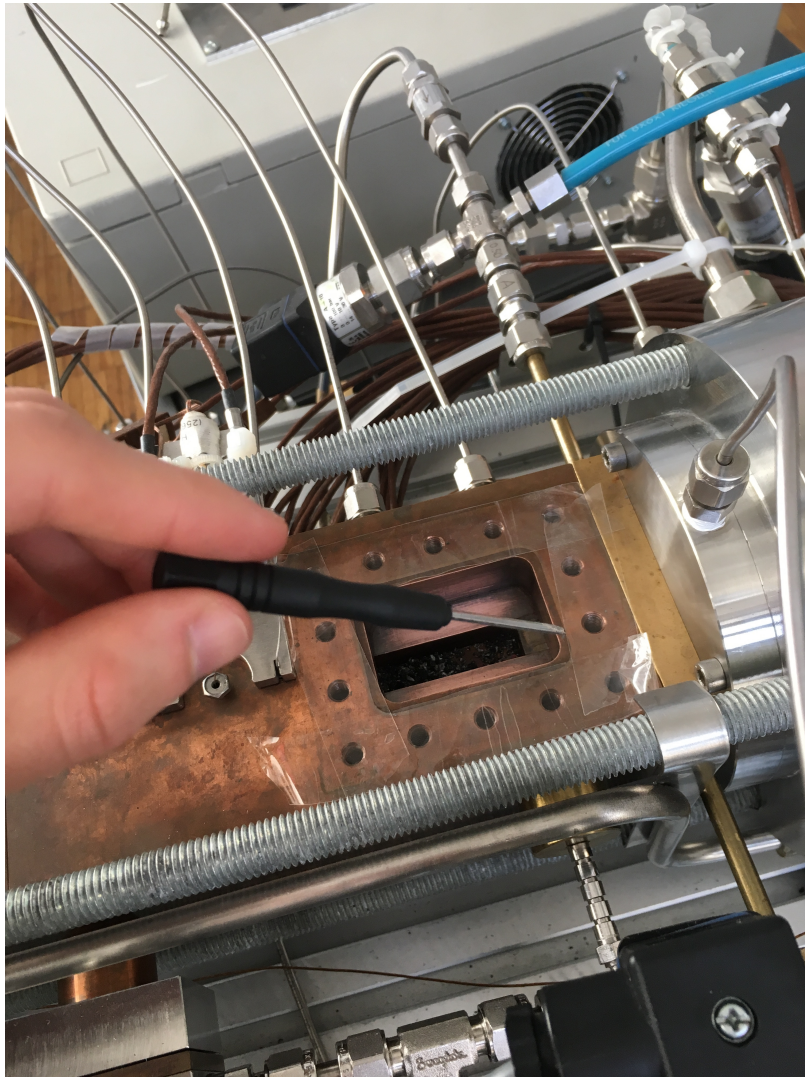
# Combustion Chamber Photos



Figure C.1: Camera optical bench



**Figure C.2:** Optical access to combustion chamber



**Figure C.3:** Insertion of the quartz window into the appropriate cavity

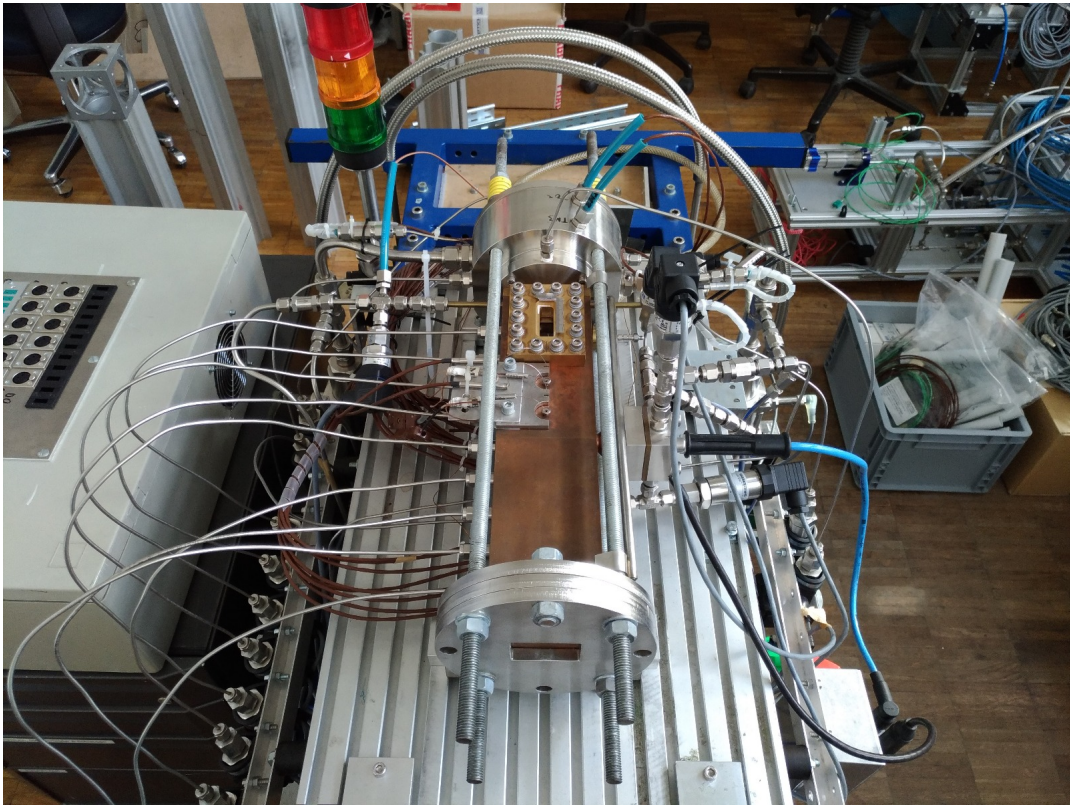


**Figure C.4:** Frontal view of MoRaP

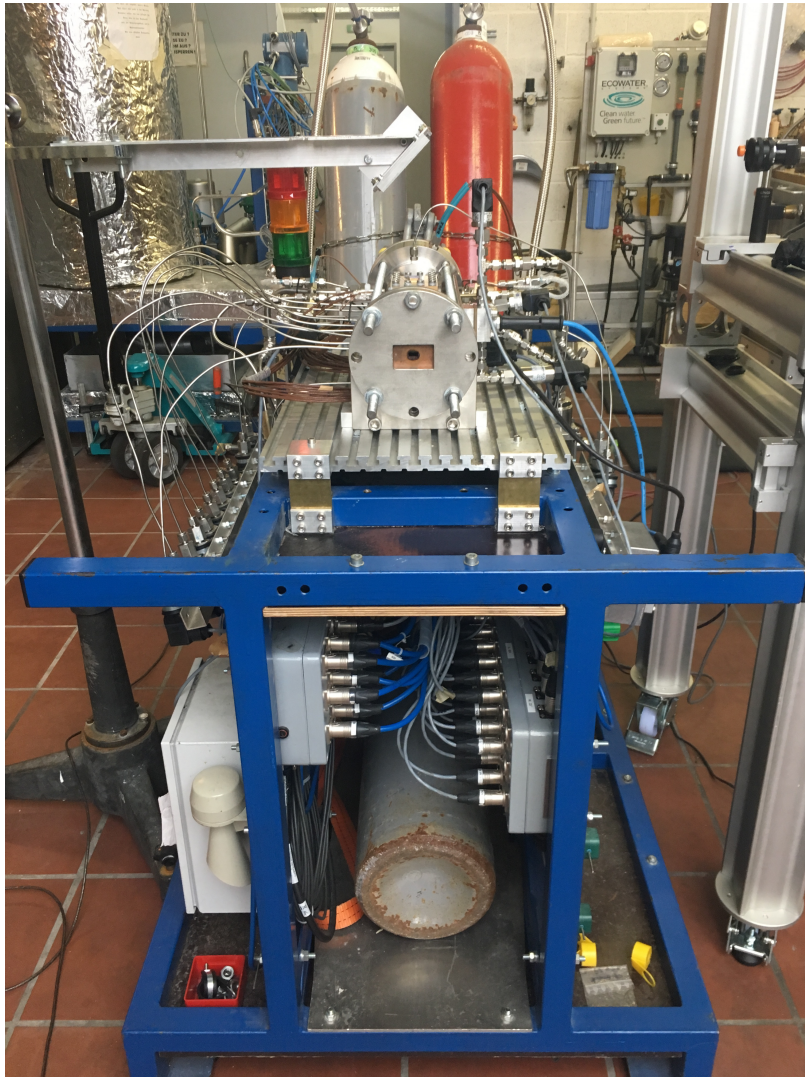


**Figure C.5:** MoRaP



**Figure C.6:** Combustion chamber during experiment